



Master Thesis

High-fidelity CFD-based Shape Optimization of a Blended-Wing-Body Aircraft for Improved Aerodynamic Performance, Considering Engine Integration Effects

Achyuth Attravanam B.Eng.
Matrikelnummer: 4997786

Examiner: Prof.Dr.-Ing. Stefan Görtz
Supervisor: Dr.-Ing. Mohammad Abu-Zurayk

Deutsches Zentrum für Luft- und Raumfahrt
Institut für Aerodynamik und
Strömungstechnik
Abteilung Center for Computer
Applications in AeroSpace
Science and Engineering - *C²A²S²E*
Braunschweig

14 August 2023

Eidesstattliche Erklärung

Hiermit erkläre ich, Achyuth, geb. am 22.06.1996, des Eides statt, die vorliegende Master-Arbeit selbstständig und ohne fremde Hilfe verfasst und keine anderen als die angegebenen Hilfsmittel verwendet zu haben.

Braunschweig, 14.08.2023

Contents

List of Figures	iii
List of Tables	iii
Nomenclature	v
1 Introduction	1
1.1 Motivation	1
1.2 State of the Art	2
2 Literature	4
2.1 Blended Wing Body	4
2.2 Aerodynamics	5
2.2.1 Navier-Stokes Equations	5
2.2.2 Mesh Generation	6
2.3 Structure Mechanics	7
2.4 Multidisciplinary Design Optimisation	7
3 Methodology	9
3.1 Modelling	9
3.2 CAD Parameterization	9
3.3 Reduce Order Models (ROMs)	12
3.4 Mesh Generation	13
3.5 Trim	15
3.6 Optimization Process	15
3.7 CFD-CSM Coupling	16
3.8 Optimization Study	17
3.8.1 Problem Statement	17
3.8.2 Design Variables	17
3.8.3 Problem Setup	18
4 Results	19
4.1 Baseline Model	19
4.2 Optimization	20
4.2.1 Engine Integration	21
4.2.2 Iteration 83	21
4.2.3 Iteration 176	24
4.3 CFD-CSM Coupling	27
5 Conclusion	30
Bibliography	32

List of Figures

1.1	Lift and Weight distribution for TAW and BWB Configurations -[1]	2
1.2	T-Tail BWB Design	3
2.1	Design Freedom -[2]	7
2.2	Cost Committed -[2]	7
3.1	Baseline Model	10
3.2	Baseline Model with Engine Integration Modification	10
3.3	Parameterization Sections	11
3.4	Airfoil Parameterization	11
3.5	Point Cloud of Blended Wing Body	12
3.6	Fluid Mesh	13
3.7	Mesh on the Wing	13
3.8	Boundary Layer with Flow for the Baseline Model	14
3.9	Y+ Contour for the Baseline Configuration	14
3.10	Structural Mesh	14
3.11	Trimming	15
3.12	Primal-Adjoint consistent Optimization Process	16
3.13	CFD-CSM Coupling	17
4.1	Baseline Model - Coefficient of Pressure (C_p) Contour	19
4.2	Baseline Model - C_p Distribution at Y = 10m from Symmetry	19
4.3	Optimization History Plot	20
4.4	Baseline Model vs Optimized Model of Iteration 83 Engine Integration Effects	21
4.5	Baseline Model vs Optimized Model of Iteration 176 Engine Integration Effects	21
4.6	C_p Contour Comparison of Baseline Model vs Optimized Model for Iteration 83	22
4.7	Comparison of (C_p) Distribution in Baseline Model and Optimized Model for Iteration 83 at Y = 10m from Symmetry	22
4.8	C_p Contour of Optimization Iteration 83 - with- vs without- Deformed Wingtip	23
4.9	C_p Distribution Plots for Optimization Iteration 83 - with- vs without- Deformed Wingtip at Y = 8, 12.5 and 17m from Symmetry	23
4.10	C_p Contour Comparison of Optimization Models for Iteration 83 vs Iteration 176	24
4.11	Comparison of C_p Distribution in Optimization Iteration 83 vs Optimization Iteration 176 at Y = 10m	25
4.12	Optimized Model of Iteration 83 and Iteration 176 Shape Comparison	25
4.13	Optimized Model of Iteration 83 and Iteration 176 Shape Comparison at X = 18.5m	25
4.14	C_p Distribution Comparison of Optimization Models for Iteration 83 vs Iteration 176 at Y = 8, 12.5 and 17m from Symmetry	25
4.15	Comparison of C_p Contour for Optimization Iteration 176 with and without Wingtip Deformation	26
4.16	Cp Distribution Plots for Optimization Iteration 176 - with- vs without- Deformed Wingtip at Y = 8, 12.5 and 17m from Symmetry	27
4.17	Deformation of the Baseline Model	27
4.18	Deformation of the Iteration 83 Model	28
4.19	Deformation of the Iteration 176 Model	29

List of Tables

1.1	Top Level Aircraft Requirements	2
1.2	Baseline Configuration Data of Airbus A320	2
1.3	Reference Values	3
3.1	Design Variables	17
3.2	Reference Parameters	18
4.1	Baseline Model Results	20
4.2	Results Comparison for Iteration 83	21
4.3	Results Comparison of Iteration 83 - with- vs without- Wingtip Deformation	22
4.4	Results Comparison for Iteration 176	24
4.5	Results Comparison of Iteration 176 - with- vs without- Wingtip Deformation	26
4.6	Results of CFD-CSM Coupling for Baseline Model	28
4.7	Results of CFD-CSM Coupling for Iteration 83 Model	28
4.8	Results of CFD-CSM Coupling for Iteration 176 Model	29

Nomenclature

Latin Symbols

Ma	Mach Number
Re	Reynolds Number
y^+	Dimensionless Wall Distance
Cf_x	Aerodynamic Forces in X
Cf_z	Aerodynamic Forces in Z
Cm_y	Aerodynamic Moments
x/c	Thickness to Chord Ratio
J	Objective Function
X_{LB}	Lower Bounds
X_{UB}	Upper Bounds
$g(\mathbf{x})$	Inequality Constraints
$h(\mathbf{x})$	Equality Constraints
C_L	Coefficient of Lift
C_D	Coefficient of Drag
C_p	Coefficient of Pressure
S_L	Lifting Surfaces
Z^{error}	Weight of Least Squares
K	Stiffness Matrix
g_f, f	External and Inertial Forces
y	Displacement
\vec{W}	Conserved Flow Variables
\vec{F}	Total Flux
\vec{F}_c	Convective Flux
\vec{F}_v	Viscous Flux
P, P_n	Production Term
D, D_n	Wall Destruction Term
T	Trip Term

Greek Symbols

ρ	Density, [kg/m^3]
μ	Dynamic Viscosity, [kg/ms]
σ	Stress, [N/m^2]
τ	Shear Stress, [N/m^2]
α	Angle of Attack (AoA)
α_{HTP}	Angle of Incidence

δ_y CSM Displacements

Acronyms

<i>BWB</i>	Blended Wing Body Configuration
<i>TAW</i>	Tube and Wing Body Configuration
<i>TLARs</i>	Top Level Aircraft Requirements
<i>MTOM</i>	Maximum Takeoff Mass
<i>OEM</i>	Operating Empty Mass
<i>TSFC</i>	Thrust Specific Fuel Consumption
<i>CFD</i>	Computational Fluid Dynamics
<i>CSM</i>	Computational Structure Mechanics
<i>NSE</i>	Navier Stokes Equation
<i>RANS</i>	Reynolds Averaged Navier Stoke Equation
<i>SA</i>	Spalart Allmaras
<i>UAV</i>	Unmanned Aerial Vehicle
<i>MDO</i>	Multidisciplinary Design Optimization
<i>MDA</i>	Multidisciplinary Design Analysis
<i>XDSM</i>	eXtended Design Structure Matrix
<i>MDF</i>	Multidisciplinary Feasible
<i>IDF</i>	Individual Discipline Feasible
<i>CO</i>	Collaborative Optimization
<i>DOE</i>	Design of Experiments
<i>SVD</i>	Singular Valued Decomposition
<i>SIAM</i>	Schall-Immissions-Armes Mittelstreckenflugzeug

Acknowledgements

I would like to thank Prof. Dr.-Ing. Stefan Görtz for providing me with the opportunity to work on the DLR-SIAM project, which is the current research in the aircraft industry, and I would also like to thank DLR, Braunschweig for providing me with the necessary resources and equipment to complete my master thesis. I would like to express my deepest gratitude to my supervisor Dr.-Ing. Mohammad Abu-Zurayk for not just guiding me during the thesis but also for imparting invaluable knowledge along with feedback and research skills required the project.

I would also extend my gratitude to Mr. Dennis Keller for providing me with guidance and feedback during the thesis, whose assistance was crucial during the research. I would like to extend my sincere thanks to Mr. Fabian Volle, Ms. Anjali Balani, and Mr. Patrick Wegener for providing me with the resources, technical support, and feedback and guiding me during the thesis. At last, I am grateful for the opportunity to contribute to the field of aircraft design optimization. I hope this work serves a meaningful contribution.

Abstract

Multidisciplinary Design Optimization has gained huge attention in the design of aircraft. Implementation of such new numerical methods provides insight into the interaction between multiple disciplines which are important in designing unconventional designs such as Blended Wing Body (BWB). This study is an extension to the DLR - SIAM project (Schal-Immisions-Armes Mittlestreck-Flugzeug eng: low-noise-immision medium-range aircraft), which deals with the shape optimization of the Blended Wing Body (BWB) to improve its aerodynamic efficiency, by including the engine integration effects. The goal of the SIAM project is to bring the BWB aircraft into service by 2035.

The Blended Wing Body design is taken from the resulting T-Tail configuration of the SIAM project. To deal with this problem, a gradient-based optimization method is used and to streamline the process, two parametric CAD-ROMs are used. One for the HTP-angle for the trim process of the aircraft and another CAD-ROM for the shape optimization. The problem is an unconstrained optimization with implicit trim constraints. Due to an unsuitable engine model, the trim process was not implemented during optimization. For shape optimization, a high-fidelity flow computation is performed with a powered engine. This study is also extended by implementing CFD-CSM coupling, which is a Multidisciplinary Design Analysis (MDA) for the critical optimization design points, where the deformation of the wing is calculated from the aerodynamic loads.

Chapter 1

Introduction

1.1 Motivation

In recent years, with the advancements in aircraft technology, air travel has become one of the safest and largest means of transportation. Global air traffic has been steadily increasing every year, and according to the website statistica [3] the number of flights performed in the year 2019 was 38.9 million and is forecasted to increase even more. With the increasing demand for air travel, it is important to make flights as efficient, economical, and carbon-neutral as possible. Currently, the estimation of annual global emissions from commercial aviation is about 2.5% and Europe has envisioned the Flightpath 2050 which is a goal to reduce 75% of CO_2 emissions per passenger kilometer, 90% reduction in NO_x and 65% in noise reduction compared to the typical new aircraft in the year 2000 [4]. To achieve this goal, pushing the design of an aircraft from a conventional (Tube and Wing - TAW) to an unconventional (Blended Wing Body - BWB) shape is necessary to explore the performance of unconventional new designs. The design of the Blended Wing Body has a huge untapped potential for increasing aerodynamic efficiency, reducing fuel burn, and reducing the noise of the aircraft. On the Tube and Wing configurations, the engines are generally placed under the wing, or attached to the fuselage behind the wing. In the first design, the noise emitted by the aircraft travels toward the ground, and it disrupts the flow over the wing as well due to the pylon and engine. The second design has the advantage of clean flow over the wing, although the engine is still exposed to the ground. With the advantage of a large fuselage of the Blended Wing Body design, the engine can be mounted on the top of the fuselage thus mitigating the noise to travel towards the ground, and with the clean wing the flow is not disrupted thus improving the efficiency.

The BWB design has another advantage in the field of weight and lift distributions. On the Tube and Wing design configuration, the weight distribution is higher on the fuselage, and the lift distribution is mostly restricted to the wings. This creates a bending moment on the wing thus the wing root should be structurally reinforced which adds more weight. Whereas for the Blended Wing Body configuration, as the lift and weight distribution is spread across the body [1], the bending moment is relatively less as seen in the figure: 1.1.

As the conventional TAW configuration is well established, further increase in overall efficiency is rather limited. On the other hand, despite the advantages of Blended Wing Body configurations, there are disadvantages for which further research is required. The BWB is sensitive to gust forces due to lower loading on the wing. With the wide body, multiple columns of passenger seats can be placed with which evacuation from the flight becomes difficult and degraded comfort due to windowless cabin, thus satisfying airworthiness is difficult. For the tailless aircraft, the problem of recovering from tumbling is of huge concern [5].

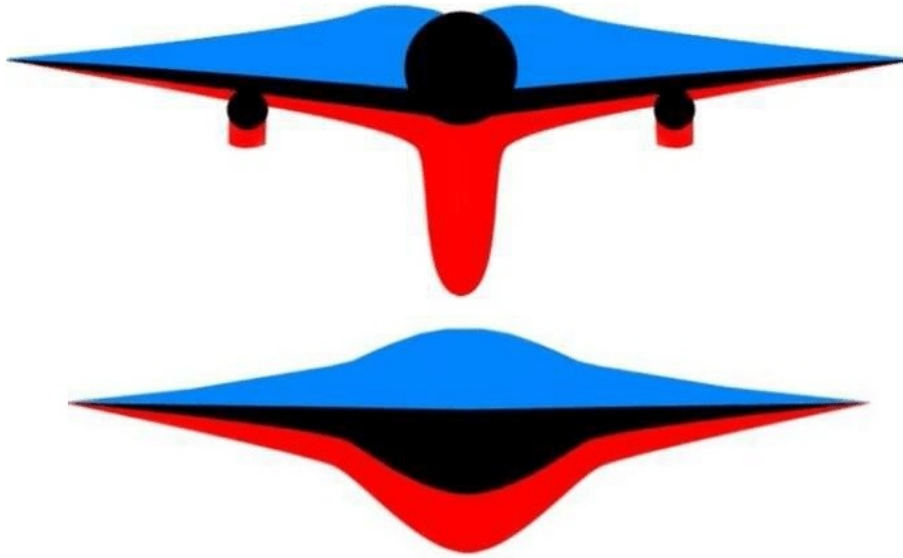


Figure 1.1: Lift and Weight distribution for TAW and BWB Configurations -[1]

1.2 State of the Art

This project is an extension of the project DLR SIAM (Schal-Immisions-Armes Mittlereckflugzeug eng: low-noise-immission medium range aircraft) [6], which mainly focuses on reducing noise emission. The Top Level Aircraft Requirements (TLARs) of the SIAM project are based on Airbus A320 which are shown in the table 1.1.

Table 1.1: Top Level Aircraft Requirements

	Unit	Value
Design Mach number	[-]	0.78
Design Range	[nm]	2600
Design payload	[t]	17.1

At these TLARs, the baseline configuration of the BWB aircraft model is designed. The Airbus A320 serves as a reference for the evaluation of efficiency and potential for noise reduction. The baseline configuration of the Airbus A320 aircraft is equipped with advanced materials and noise-reduction technologies from the project Low Noise ATRA [7]. This baseline configuration is also installed with an ultra-high bypass ratio engine which is significantly improved in recent decades in both efficiency and noise. The BWB aircraft is optimized for minimum fuel consumption and the baseline configuration data along with the reference values are shown in the table 1.2 and 1.3.

Table 1.2: Baseline Configuration Data of Airbus A320

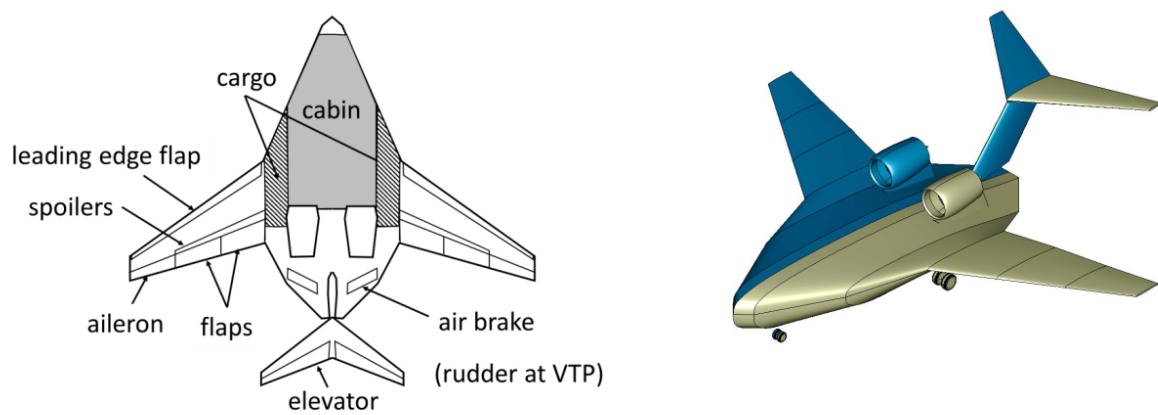
	Unit	Value
MTOM	[t]	74.2
OEM	[t]	43.2
L/D	[-]	17.5

The SIAM project includes the basic layout of the BWB along with an extensive study of its handling qualities and approach trajectory evaluation, noise evaluation, planform variation, and design variations. After considering various designs, the T-tail design was selected which is shown

Table 1.3: Reference Values

	Unit	Value
Reference Area	$[m^2]$	348.1
Reference Length	[m]	5.35
Reference Point (x)	[m]	14.95

in figure 1.2, as it has the most promising results. The SIAM project also concludes the studied Hybrid Wing Body (HWB) configuration, is designed as naturally stable and it is possible to control without artificial support. It is also mentioned that by using HiFi-optimization, there is a high probability of increasing the lift coefficient [6]. This study being an extension of the SIAM project, focuses on shape optimization of the BWB body with T-tail configuration at the above-mentioned design conditions.

**Figure 1.2:** T-Tail BWB Design

Chapter 2

Literature

In this chapter, the theory behind the problem is reviewed. The first section 2.1 deals with the background of the Blended Wing Body design, and in the second section 2.2 the basics of CFD along with the mesh generation are reviewed. In the next section 2.3, the basics of CSM are studied. In the last section 2.4 the fundamentals of MDO are outlined.

2.1 Blended Wing Body

The idea of a Blended Wing Body (BWB) design of an aircraft stems from the idea that both the wing and the fuselage should contribute to generating lift. As the lift generated is directly proportional to the area of the lifting surface (S_L), the BWB has the potential to produce significantly higher lift when compared to the traditional Tube and Wing configuration (TAW), thus increasing the aerodynamic efficiency of the aircraft.

$$L = \frac{C_L \rho v^2 S_L}{2} \quad (2.1)$$

The concept of BWB was studied and evaluated in a preliminary design study conducted at McDonnell Douglas when Dennis Bushnell of NASA Langley's research center posed an important question "Is there a renaissance for long haul transport?" [8]. With funding from NASA at McDonnell Douglas, the initial study was to develop and compare the advanced technology of subsonic transport for the design mission for 800 passengers and 7000 nautical mile range with the Mach number of 0.85. The study also involved the design of the body, where the pressurized cabin compartment was designed as an adjacent parallel tube which is a lateral extension of the double bubble concept. This study is a chronicle for the future development of the BWB aircraft configuration, as BWB-450 (with a payload of 450 passengers) is compared with Airbus A380, showed a striking result of 32% less fuel burn per passenger [8].

Boeing also worked on developing a BWB model as an unmanned aerial vehicle (UAV), which was a joint program between Boeing, NASA, and Air Force Research Laboratory, where Boeing was responsible to deliver X48B. The goal of the program was to reduce emissions, and noise, improve the performance of the aircraft, and thus develop a highly fuel-efficient aircraft. The main goal of the flight test was to verify and validate the control systems of X48B. For X48B, Boeing has developed two models, one for wind tunnel testing and an actual airplane which is 8.5% scale of the actual model for the flight test. In the X48B and the next project X48C, the main problem of pitch tumble was tested as it is a problem with tailless BWB configuration. To resolve this Boeing has implemented Angle of Attack (AoA) limiters so that the flight does not lead to unstable and uncontrollable flight conditions. It was also mentioned that the performance of X48B test flights was good and the flight control system was in fact feasible for the BWB [9].

Other aircraft manufacturers such as Airbus, Bombardier, and JetZero are currently working on developing aircraft with BWB configuration. Airbus is working on the project MAVERIC (Model Aircraft for Validation and Experimentation of Robust Innovative Controls) which is a blended wing scaled model as a technological demonstrator [10]. Bombardier is working on the EcoJet project using BWB configuration, with technologies as such, the company plans to achieve zero emissions by 2050 [11]. The new company JetZero which was established in the year 2020 by the engineer who originally developed BWB configuration, Dr. Robert Liebeck, is doing tremendous research in the BWB configuration in project Z5. The Z5 design is optimized for a range of 5000 nautical miles, with a payload of 250 passengers. It was stated that Z5 would require half the power of the Boeing 767 aircraft with half the weight and Z5 can also carry up to twice the amount of fuel when compared to Boeing KC 46 tanker on a maximum range mission [12].

2.2 Aerodynamics

The DLR-TAU code is used to simulate the external aerodynamic flow around an aircraft model. TAU code is a CFD solver package that is built in-house by DLR which has the capability to solve Euler and Reynolds Averaged Navier-Stokes equations (RANS). TAU code was developed in Göttingen and Braunschweig back in the 1990s, and it was built to calculate 3-Dimensional flow simulations for unstructured hybrid grids with efficient parallel computing capability. TAU code is best used for complex geometries in low subsonic to hypersonic flow regimes. [13, 14].

TAU comprises three modules, namely preprocessing, solver, and grid adaptation. Since the TAU doesn't have an inbuilt mesh generator, the preprocessor needs to prepare a metric of the grid. The metric is the geometric coordinates of the nodes, volumes of dual cells, and normal vectors representing the size and orientation of the faces of the cells. Thus TAU generates a secondary grid by linking two nodes on both sides of each face to the corresponding edge of the primary grid. This secondary grid makes the solver independent of the primary grid and its elements, thus it enables the use of the multigrid technique, which is based on the agglomeration approach [13, 14].

The flow solver is based on the compressible Navier Stokes Equations (NSE) which can be extended to incompressible NSE during low Mach numbers. The NSE is solved using finite volume methods, where the flow variables are stored in the vertices of the initial grid and the fluxes are discretized using the central differences method. The gradients of the flow variables are calculated using a central method with scalar or matrix dissipation. [13, 14].

2.2.1 Navier-Stokes Equations

The flow behavior is described using Navier-Stokes equations (NSE), which are second-order nonlinear partial differential equations. It was developed by Claude-Louis Navier and George Gabriel Stokes between 1822 to 1850. The equation is derived from momentum conservation and it mathematically expresses mass balance, momentum, and energy conservation. The various terms in the Navier-Stokes equation include a local change in time, a convective term, a pressure term, and a stress term.

The general expression for solving the Navier-Stokes equation with convective fluxes is

$$\iiint_V \frac{\partial}{\partial t} \vec{W} dV + \iint_S \vec{F} \cdot \vec{n} dS = 0 \quad (2.2)$$

$$\vec{W} = \begin{bmatrix} \rho \\ \rho u \\ \rho v \\ \rho w \\ \rho E \end{bmatrix} \quad \vec{F}_c = \begin{bmatrix} \rho \vec{q} \\ \rho u \vec{q} + p \vec{i}_x \\ \rho v \vec{q} + p \vec{i}_y \\ \rho w \vec{q} + p \vec{i}_z \\ \rho H \vec{q} \end{bmatrix} \quad \vec{F}_v = \begin{bmatrix} 0 \\ \tau \vec{i}_x \\ \tau \vec{i}_y \\ \tau \vec{i}_z \\ (\tau \vec{q} - k \Delta T) \vec{i} \end{bmatrix}$$

Where \vec{W} is the conserved flow variables which are defined as density ρ , momentum $\rho u, \rho v, \rho w$, and total energy ρE . The total flux of the flow \vec{F} is the sum of convective \vec{F}_c and viscous flux \vec{F}_v .

The Spalart Allmaras (SA) is a 1-Equation transport model which is derived especially for aerodynamic applications and low Reynolds number applications. The model has a single governing kinematic equation to describe viscous eddy current flow. The model is particularly used to capture boundary layer flow with adverse pressure gradients. A major limitation of SA is its unreliability in describing the decay of turbulent flows, also its applicability beyond the wall-bounded systems is unproven [15]. The SA is derived to be

$$\frac{D\tilde{\nu}}{Dt} = P - D + T + \frac{1}{\sigma} [\nabla \cdot ((\nu + \tilde{\nu}) \nabla \tilde{\nu}) + c_{b2} (\nabla \tilde{\nu})^2]$$

A variation of SA is the neg-Spalart Allmaras model which is primarily developed to address the issue of under-resolved grids and non-physical transient states where discretization of the model leads to undesired results. The SA model only admits non-negative solutions provided the boundary and initial condition is non-negative. Although there are a few scenarios on coarse grids and transient states where the turbulent solution tends to decrease below zero. These scenarios often occur at edge of boundary layers and at wakes, where the rapid transition from large inner levels to small outer levels can result in undershoots for discrete solution which results in negative solutions. The general practice is to clip the updates thus eliminating negative solutions. The method of clipping the updates prevents the convergence of PDE residuals and obstructs the effort to quantify the discrete truncation and solution errors. The solution to this issue is the neg-SA, where negative turbulent solutions of SA $\tilde{\nu}$ produce zero eddy viscosity. The neg-SA is energy stable. The analytical solution is non-negative provided non-negative boundary condition is provided [16]. The neg-SA is given as

$$\frac{D\tilde{\nu}}{Dt} = P_n - D_n + \frac{1}{\sigma} \nabla \cdot [(\nu + \tilde{\nu} f_n) \nabla \tilde{\nu}] + \frac{c_{b2}}{\sigma} (\nabla \tilde{\nu})^2$$

2.2.2 Mesh Generation

The mesh for the BWB model is generated using ANSA pre-processor software which is developed by BETA CAE systems. It has the ability to generate mesh for both structure and fluid simulations and it has various environments in which size fields for meshes can be generated, which is used to build fine mesh in certain predefined areas. It has also the ability to perform CAD clean-up along with mesh quality control. Another interesting environment in ANSA is to generate mesh morphing and optimization. For the CFD application, ANSA can build prismatic layers based on y^+ calculation to capture near-wall flow i.e. boundary layer phenomena accurately, and in the farther area from the wall for farfield calculations, it can build an unstructured grid for faster computation[17].

2.3 Structure Mechanics

The structure simulations are solved using the finite element methods (FEM). The governing equations of the structure simulation are the equations of linear elasticity. After discretization, the governing equation becomes

$$\mathbf{R} = \mathbf{K}(\mathbf{y}) - (\mathbf{g}_f + \mathbf{f}) = 0 \quad (2.3)$$

Where the \mathbf{K} is the symmetric stiffness matrix which is given by $K = K(\mathbf{X}, z_{sizing})$, the external and inertial forces are given by \mathbf{g} and \mathbf{f} respectively and the resulting displacements are given by \mathbf{y} [18].

2.4 Multidisciplinary Design Optimisation

Multidisciplinary Design Optimization (MDO) is defined as “a methodology for design and analysis of complex engineering systems and subsystems which coherently exploits the synergism of mutually interacting phenomena” by AIAA during the 30th fluid dynamics conference in 1999 [19]. To solve any complex system such as the design of an aircraft where multiple disciplines are involved, designing sequentially does not give the most efficient design. This is due to the lack of interaction between multiple disciplines. Almost all of the commercial aircraft that were built up to the year 2000 have been designed sequentially, and in current times, MDO is not yet completely integrated into aircraft design but to build an unconventional design such as BWB configuration, multiple disciplines should be coupled which is possible through MDO.

The advantage of using MDO is to reduce the time during the design phase by coupling multiple disciplines whereas the sequential design involves design loops that require a lot of time. It also helps to retain design freedom for a longer time in the design process, with which more knowledge of the design can be studied before freezing the design. MDO also provides an edge to a designer as it provides the ability to perform trade-off studies between disciplines. The brief description of design freedom and the cost of MDO as shown in the figures: 2.1 and 2.2 was mentioned by Mavroudi.D [2]

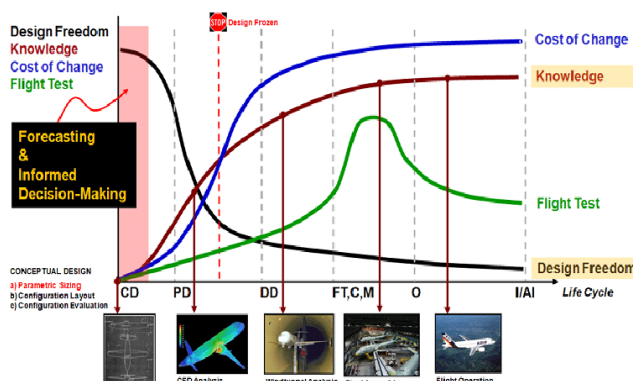


Figure 2.1: Design Freedom -[2]

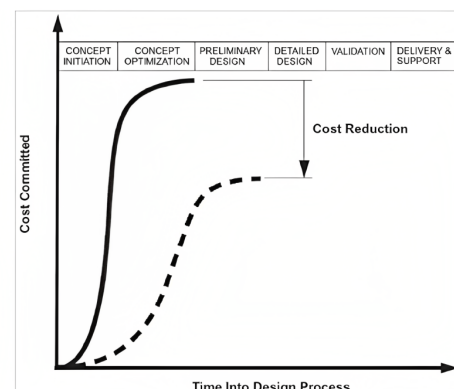


Figure 2.2: Cost Committed -[2]

Any MDO problem is defined using the standard problem formulation which involves objective function, design variables, constraints, and upper and lower bounds.

$$\min_x J(\mathbf{x}) \quad (2.4)$$

$$s.t. \quad g(x) \leq 0 \quad (2.5)$$

$$h(x) = 0$$

$$\mathbf{x}_{LB} \leq \mathbf{x} \leq \mathbf{x}_{UB} \quad (2.6)$$

$$J = [J_1(\mathbf{x}) \dots J_z(\mathbf{x})]^T \quad (2.7)$$

$$\mathbf{x} = [x_1 \dots x_i \dots x_n]^T \quad (2.8)$$

$$g = [g_1(\mathbf{x}) \dots g_{m_1}(\mathbf{x})]^T \quad (2.9)$$

$$h = [h_1(\mathbf{x}) \dots h_{m_2}(\mathbf{x})]^T Cl \quad (2.10)$$

The objective function is defined in the formulation as $J(\mathbf{x})$, where convention dictates the minimization of the objective function, although one can maximize it depending on the problem statement. The constraints are given as $g(\mathbf{x})$ as the inequality constraint and $h(\mathbf{x})$ as the equality constraint. The upper bounds \mathbf{x}_{UB} and lower bounds \mathbf{x}_{LB} of the design variable \mathbf{x} are also necessary as they do not allow the design variables into non-feasible design space. The objective function can also be a vector forming a multiobjective problem.

There are two major approaches to solving complex MDO problems, which are gradient-free and gradient-based methods. To solve an MDO problem, architecture is important as it defines the order in which the algorithms are executed, it helps to visualize the data and process flow, and to capture it an extended design structure matrix (XDSM) diagram is required. A few of the commonly used architectures are Multidisciplinary Feasible (MDF), Individual Discipline Feasible (IDF), and Collaborative Optimization (CO) [20].

Chapter 3

Methodology

This chapter outlines the procedure used in the study. In section 3.1, CAD modeling is discussed, then the CAD parameterization is summarized in section 3.2. For the optimization, the CAD-ROM and mesh generation are discussed in the sections 3.3 and 3.4 respectively. Then the trim, optimization process, and CFD-CSM coupling are reviewed in the sections 3.5, 3.6, and 3.7 respectively. In the last section 3.8 a brief description of the optimization study is outlined which includes the problem statement, design variables, and problem setup.

3.1 Modelling

The CAD model of the blended wing body (BWB) as shown in figure: 3.1 is made in CATIA V5 as an assembly of various CAD parts. The various parts of the model are the main wing model which consists of the fuselage and wing, an engine integration model which is an extension of the main wing model used to generate the channel for the airflow, an engine model, a pylon model, and HTP and VTP models for the stability of the aircraft. The main wing model is made of various airfoil shapes which are used to build the skin of the aircraft using the loft command. Using the fuselage and the nacelle, a channel is generated under the engine on the fuselage in such a way that the designed engine integration section has better aerodynamic performance. During optimization to include the engine integration effects, the engine integration section is also parameterized. To make the CAD model more robust to optimization, the width of the engine integration section is extended as the optimizer would have a higher degree of freedom to generate a better result in reducing the drag. The updated baseline model with a larger width of the engine integration section can be seen in the figure: 3.2 .

3.2 CAD Parameterization

The CAD parameterization is executed in CATIA using the 3D curve feature [21]. The 3D curve is a B-Spline curve that can be defined using control points, where changing the control point modifies the curve. Using the 3D curve, an airfoil shape can be generated by modeling the upper and lower surfaces of the airfoil separately, and to model the 3D curve accurately as an airfoil, 10 control points are used to generate each side of the airfoil. Each control point is fixed in the X coordinate and it can only be adjusted in the Z coordinate, thus reducing the dimensions of the problem. For parameterizing the airfoil accurately, the control points are clustered near the leading edge as it needs to capture its curvature.

Each parameterized airfoil is then fitted onto the original airfoil by using optimization methods that are available in CATIA. The optimization method tries to minimize the least squares solution between the airfoil coordinates and the projection of the airfoil coordinates on the 3D curve

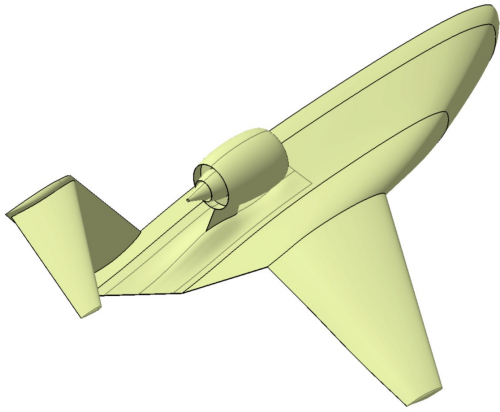


Figure 3.1: Baseline Model

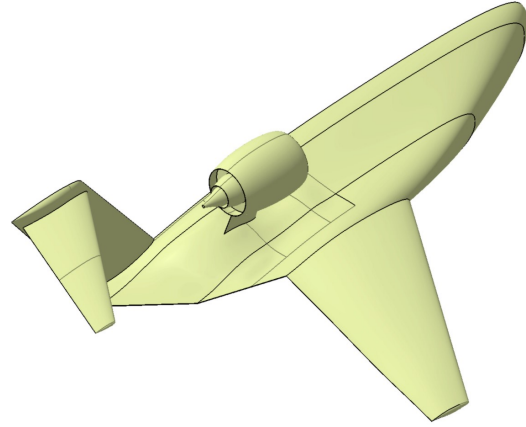


Figure 3.2: Baseline Model with Engine Integration Modification

(which is an approximation or reconstruction of the airfoil shape). The least-square solution is given by

$$z^{error} = \frac{1}{N} \sum_{i=1}^N w_i (z_i^{target} - z_i^{approx})^2 \quad (3.1)$$

where w_i is the weight for the least squares. The minimization of the least squares solution is one of the well-studied methods which provide acceptable results for the reconstruction of the airfoil geometry. This method is also used as a benchmark to test various reconstruction cases in the paper by D.A. Masters and N.J. Taylor [22]. The solution of the least squares method is deemed acceptable when

$$z^{error} < \begin{cases} 4 * 10^{-4}, & \text{if } x/c < 0.2 \\ 8 * 10^{-4}, & \text{if } x/c > 0.2 \end{cases} \quad (3.2)$$

The minimization method used in CATIA is the simulated annealing algorithm which is global stochastic search algorithm that evolves towards local search as time progresses [23]. This algorithm provides quick results, as the goal of curve fitting is to minimize the distance between the actual points and their projected points without any constraints, where the design variables are the control points of each side of the airfoil.

The parts considered to parameterize the Blended Wing Body model are the main wing, pylon, engine integration, and HTP. As the main wing and pylon are made of airfoils, the extracted sections for parameterization are also the shape of airfoils. On the main wing, four sections on the fuselage and seven sections on the wing are considered as shown in the figure: 3.3. The sections on the wing are more clustered towards the wing root and wing tip making the wing shape sensitive to flow. As each section contains 20 control points (10 for each side of the airfoil), 220 control points are generated for the main wing model. Twist angles are also considered for the sections on the wing as they greatly influence the flow. Although there are seven sections on the wing, the twist angle for the wing root is not considered as changing it changes the fuselage shape as well, which is unphysical. With six twist angles and 220 control points of the airfoils, the total design parameters for the main wing model is 226. The parameterization of the airfoil along with the control points can be seen in the figure: 3.4. The first and the last points of the airfoil are not included during reconstruction and optimization as it changes the airfoil's leading edge and trailing edge, which is not required.

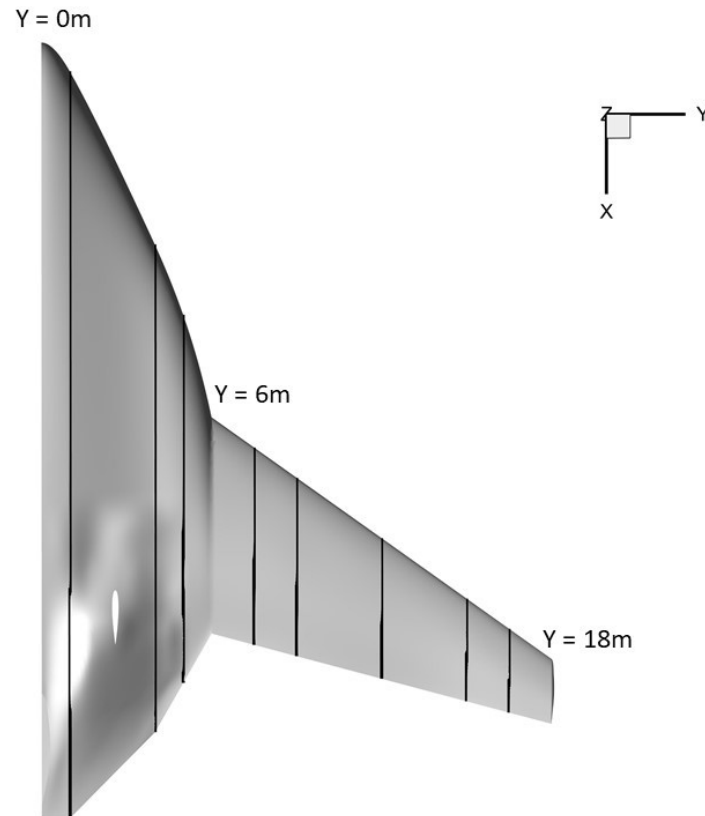


Figure 3.3: Parameterization Sections

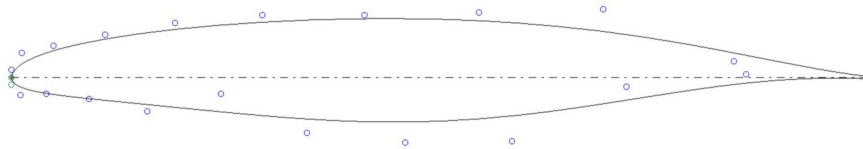


Figure 3.4: Airfoil Parameterization

The pylon model is also considered for parameterization, as it connects the engine to the fuselage where a huge shock was observed during preliminary analysis due to the presence of the engine. Only one section of the pylon is considered which also has the airfoil shape. Thus parameterizing the pylon requires 20 control points. For engine integration, five sections are considered to reconstruct the skin. Similar to the airfoil parameterization, the 3D curve feature is used along with optimization to generate a parameterized section. Each section is considered to have 11 control points, thus producing 55 design variables.

The HTP model is also parameterized to adjust its angle of incidence. This is particularly used during the Trim process. The total design variables considered for the BWB model is 302 along with the HTP angle. For each part, one design table is generated so that each model can be easily updated with different configurations thus modifying the whole geometry. From the assembled BWB model, various parts are again extracted to generate a point cloud. On each extracted part isoparametric curves are generated equidistant from each other, then on every isoparametric curve, equidistant points are generated creating a point cloud for the geometry. The extracted point cloud for the baseline configuration model can be seen in the figure: 3.5.

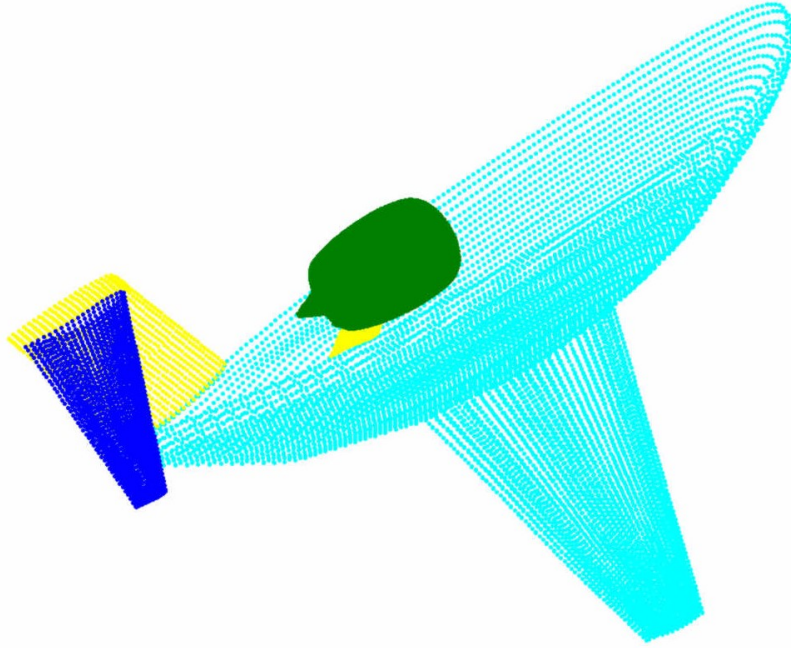


Figure 3.5: Point Cloud of Blended Wing Body

3.3 Reduce Order Models (ROMs)

Reduce Order Models (ROMs) in the branch of unsupervised learning is a method used to reduce problem complexity, especially when dealing with large degrees of freedom. The goal is to reduce the dimensionality of the problem to much lower dimensions and yet show the results with correct physics making the simulation computationally inexpensive with faster solving time. The technique most commonly used in ROMs is the Proper Orthogonal Decomposition (POD), where the matrix is decomposed using either Eigenvalue Decomposition when the matrix is square or Singular Value Decomposition (SVD) when the matrix is rectangular. Using these techniques, the modes can be extracted where the first couple of modes are more dominant as they contain majority of reconstructed data. The data can be reconstructed more accurately just by including more modes.

The CAD-ROM is a part of the SMARTy (Surrogate Modelling for AeroData Toolbox) software package which is developed in-house by DLR [24]. The CAD-ROM approach was originally developed by Bobrowski et al [25]. The CAD-ROM is used during the optimization as the ROM represents a parametric CAD generator, it generates new shape displacement field with new design variables from every iteration. Thus the CAD-ROM is used to streamline the optimization process.

SMARTy also supports different Design of Experiments (DOE) methods for data acquisition such as Latin Hypercube Sampling and SOBOL Sampling. In Latin Hypercube Sampling (LHS), the data is randomized by dividing the space into an equal number of portions of equal marginal probability and sampling one from each interval. Therefore no two samples are from the same interval, thus making the sample diverse and it covers the entire space [26]. On the other hand, SOBOL sampling belongs to quasi-random sequences that can generate samples of multiple parameters uniformly over multi-dimensional parameter space. While generating a new sample, the SOBOL algorithm considers previously sampled points, thus points are not clustered. A discrepancy metric is used to assess the performance of sampling methods, where the lowest discrepancy is found for SOBOL sampling as it distributes the sampling points evenly on the design space [27]. Therefore using the SOBOL sequence, the design space is sampled for the

CATIA to generate a point cloud of the model which is used to generate the CAD-ROM.

Two CAD-ROMs are necessary for the optimization, one for the HTP angle of incidence and the other for the whole aircraft. A separate ROM for the HTP angle is required as it is used for trimming the aircraft to balance the forces. To generate a CAD-ROM, the Design of Experiments (DOE) needs to be performed on each design table that is used by the respective model. For the SOBOG sampling, the original design parameters along with their names, lower bounds, and upper bounds are necessary to sample the design space. The lower bounds and upper bounds are considered to be ± 20 mm with respect to the original design parameters. For twist angles, a small deflection of ± 3 deg is considered. For the whole aircraft, 6000 sample points are generated for each design table, as the total number of design parameters is 301. With a higher number of design parameters, higher sampling is necessary so that the CAD-ROM can generate better results. The point clouds that were extracted from the CAD models are from 92.7% of the sampled design space, thus generating 5565 variations of point cloud data from the sampled points.

For the HTP angle of incidence, 1000 sampling points are generated as the design parameter is only one. The point clouds extracted from the CAD models are from 100% of the sampled design space, thus generating all 1000 variations of the point cloud data. This percentage shows the capability of the CAD models in generating the point clouds. The point cloud data was extracted by adding the sampled points back into respective CAD models and a macro was used to run each sampled configuration and the respective modification of point cloud data was saved as a text file.

3.4 Mesh Generation

The mesh generation is performed using ANSA pre-processor. For the fluid mesh, an outer hemispherical domain for the farfield is created with the symmetric plane connected to the aircraft model. Using the batch mesh option in ANSA, individual parts of the model were meshed simultaneously with different mesh settings. ANSA has a powerful geometrical feature recognition tool, which is used to detect the leading edges, trailing edges, and sharp edges. Using this tool, a fine mesh with gradual coarsening is generated in the leading edge area, which can be varied using a growth factor along the chord length. A similar treatment of generating a fine mesh is also used for sharp edges, for higher flexibility of mesh refinement. Using the same tool, ANSA also generated additional number of rows in the trailing edges and a gradual mesh coarsening from the trailing edge with growth factor is also used for quality mesh generation. The generated surface mesh can be seen in figure: 3.6, and the mesh treatment across the wing can be seen in figure: 3.7.

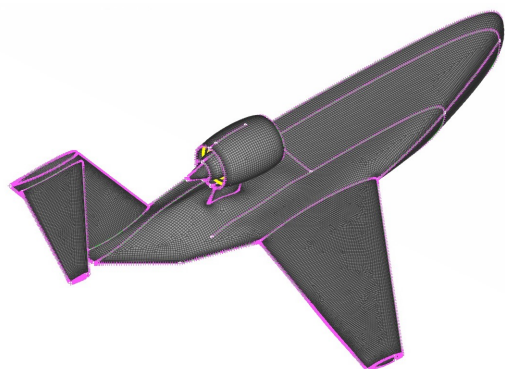


Figure 3.6: Fluid Mesh

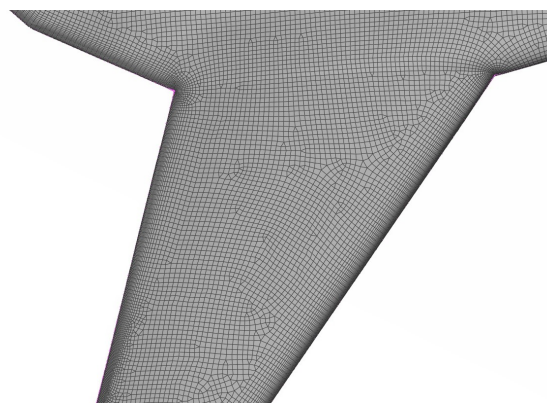


Figure 3.7: Mesh on the Wing

To capture the boundary layer phenomenon, prismatic layers are built on the surface mesh.

As the Spalart Allmaras is considered for the flow simulation, a y^+ of 1 is selected for mesh generation. With the Reynolds number of 30 million, the first cell height is calculated to be 0.0088 mm and with the growth factor of 1.2 and the number of layers being 38, the total cell height of prismatic layers to capture boundary layers is calculated to be 44.8 mm. The boundary layer flow with the prismatic layers can be seen in the figure: 3.8, which shows that the boundary layer of the flow is very small compared to the generated prismatic layers. With the surface mesh, prismatic layers, and unstructured volume mesh in the far field, the total number of nodes generated for the CFD mesh was around 4.2 million. The boundary layer is also validated using the Y^+ contour of the baseline model, where the Y^+ value is close to 1 for the wall-bounded flow as shown in the figure: 3.9.

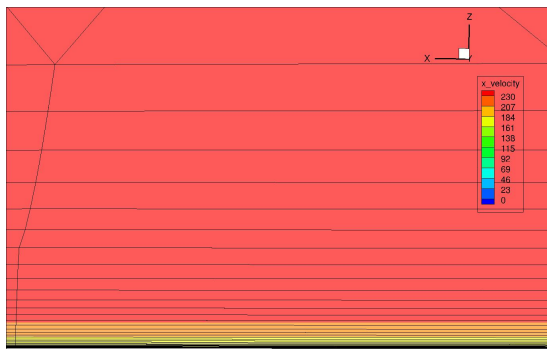


Figure 3.8: Boundary Layer with Flow for the Baseline Model

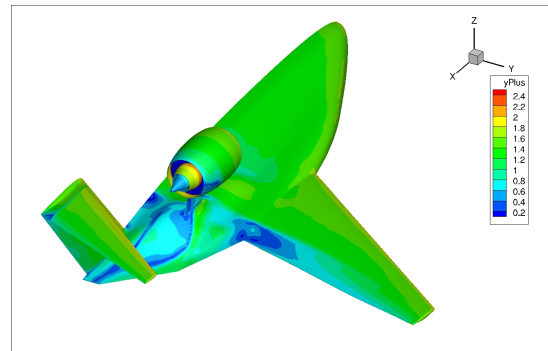


Figure 3.9: Y^+ Contour for the Baseline Configuration

For the structural solver, the whole body is considered to accurately compute the displacement of the wing. To reduce the complexity of the structural simulation, the engine is replaced by point loads, as the focus lies on the displacement of the wings. The point loads are defined by the CONM2 element and they are placed at the center of the engine and are connected to the fuselage using 1D CBEAM elements. The leading edge and the trailing edge in the structure model are excluded, as they are exterior to the wing box and don't contribute to the deflection behavior. The generated structural mesh is shown in the figure: 3.10.

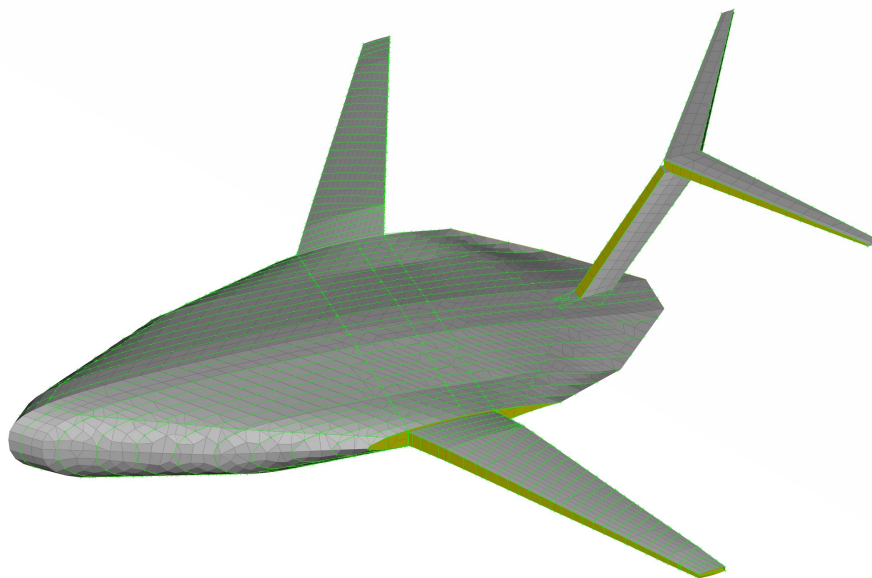


Figure 3.10: Structural Mesh

3.5 Trim

To accurately simulate flight physics, each optimization iteration needs to be trimmed where the aircraft's forces and moments at the steady state equilibrium are satisfied. The trimming is an MDO problem as it involves aerodynamic analysis of the aircraft and flight dynamics. The forces and moments which account for aerodynamic loads, gravitational loads, and thrust force, are calculated as Cf_x , Cf_z , Cm_y using TAU. The trimming is iteratively converged using Newton's optimization algorithm by changing the design parameters of the aircraft such as angle of attack α , angle of incidence α_{HTP} , and thrust. For the next trim iteration, Jacobian is calculated which is a matrix of first-order partial derivatives, and updated using the Broyden's Bad method. The convergence of the trimming process is accelerated using Aitken's method. These methods are studied for optimization process of trim in the paper published by the DLR[28].

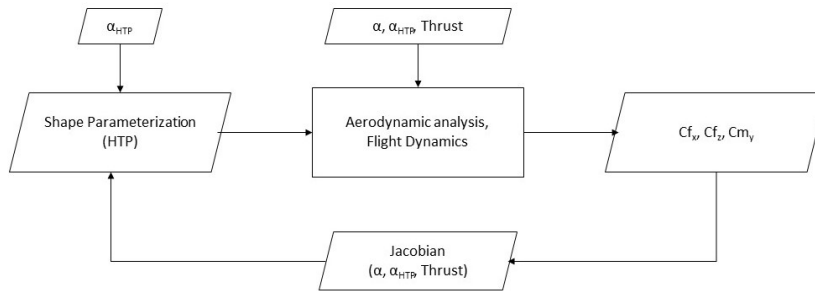


Figure 3.11: Trimming

3.6 Optimization Process

The primal-adjoint consistent optimization process is a gradient-based optimization algorithm that maximizes the aerodynamic efficiency with respect to shape design parameters. The primal and adjoint workflows are ingrained in the FlowSimulator environment which is an in-house built DLR code used specifically for parallel multiphysics simulations on HPC clusters. By replacing the CAD models using CAD-ROMs, the optimization process is streamlined, and with every iteration, a new shape displacement field for mesh deformation is generated on the supporting mesh from which geometric sensitivities are computed. For each design iteration, trimming is performed implicitly which makes the optimization feasible, which means that the optimization can be stopped after any iteration and can be resumed again as the objective functional improvements are still valuable since all constraints are met due to steady state equilibrium. The trimmed steady-state equilibrium is not used as the constraint for the optimization and since the trimming is implicit, the top-level optimizer becomes an unconstrained optimization. To compute sensitivities, the trim algorithm is replaced by the trim-correction algorithm as the unconstrained optimization needs information from the objective functional gradient to take minuscule changes in the trim into account. After the trim iteration is complete the new trim vector is suggested by the algorithm which contains the current cruise thrust request. The thermodynamic engine performance model is analyzed with which Thrust Specific Fuel Consumption (TSFC) and thermodynamic states are computed. The thermodynamic states are used to define engine boundary conditions such as inflow and exhaust [29, 28].

Since the optimization is a high-fidelity CFD-based shape optimization, several aerodynamic analysis iterations are performed for every trim parameter. The aerodynamic analysis is performed first, where it receives the current angle of attack α and the engine boundary conditions from the trim algorithm and engine model respectively. The optimization algorithm calculates the objective function and calculates gradients of objective function and design variables for the

next iteration. With the computed gradients, the CAD-ROM generates the shape displacements, where the baseline mesh is deformed by mapping the points onto the grid, along with the HTP deflect which is predicted by the Trim algorithm. The process is repeated for the next iteration by computing aerodynamic analysis for the deformed mesh [29, 28]. The optimization process is drafted in the figure: 3.12

The sensitivities of the objective function are computed with respect to shape parameters using the adjoint method. The adjoints of flow and the mesh along with the flow solvers are consistently coupled using the block-Gauss-Seidel method [29, 28].

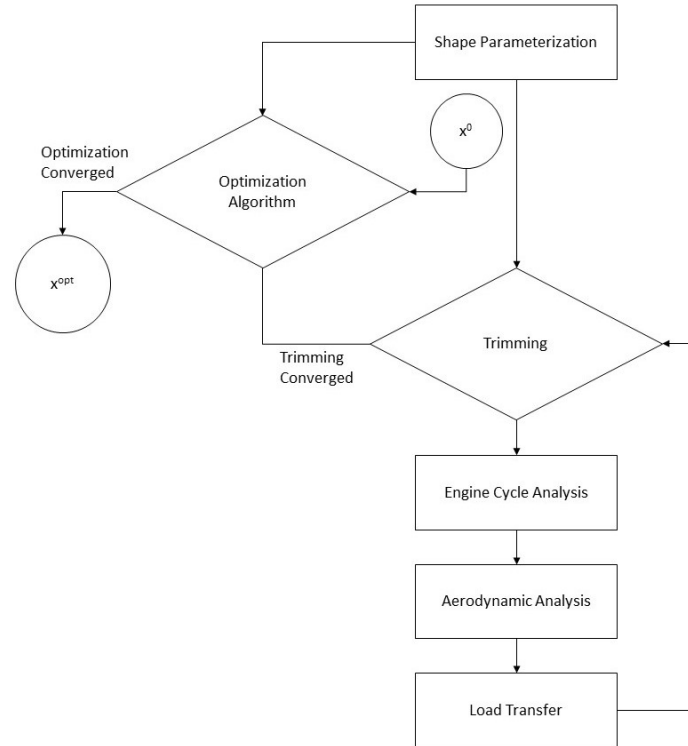


Figure 3.12: Primal-Adjoint consistent Optimization Process

3.7 CFD-CSM Coupling

The CFD (Computational Fluid Dynamics) - CSM (Computational Structure Mechanics) coupling is performed using the Airbus Lagrange suite for MDO with more focus on structural analysis which has been coupled with DLR TAU code through the FlowSimulator framework. This procedure facilitates the simultaneous optimization of airframe shape and sizing parameters to extract maximum aerodynamic performance. It is important to include structural analysis in MDO as the structural weight has an influence on overall aircraft performance and the structural properties affect the in-flight shape of an aircraft such as the flutter of the wings and thus its aerodynamic characteristics. To design a robust aircraft the interaction between the disciplines of aerodynamics and structure mechanics must be taken into consideration [18].

The coupling of CFD and CSM disciplines is achieved by iteratively solving the fluid flow and structural sub-problems in sequence. At every iteration, by solving a CFD computation, the aerodynamic forces on the solid-fluid interface are computed, which applied as the boundary conditions in the structural sub-problem. Then by solving the structure sub-problem, the resulting displacements (δ_y), which are a subset of the new structural state are reassigned back to the corresponding surface of the fluid mesh. The transferring of structural mesh to fluid mesh is

managed by surface mapping and mesh deformation [18]. The coupling of CFD-CSM is drafted in figure: 3.13

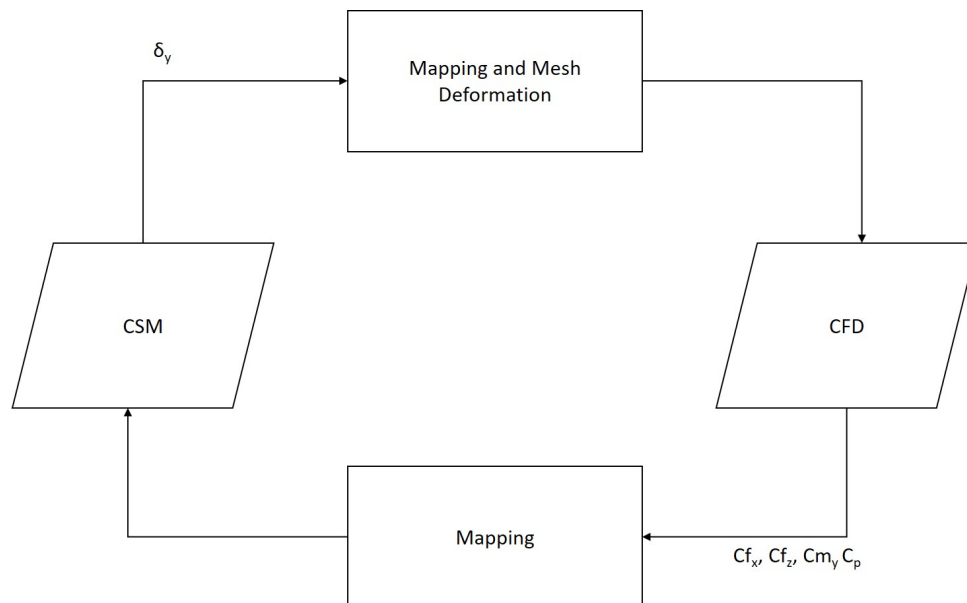


Figure 3.13: CFD-CSM Coupling

3.8 Optimization Study

3.8.1 Problem Statement

To maximize the Aerodynamic Efficiency of a Blended Wing Body aircraft T-tail configuration by changing its geometry parameters by including engine integration effects while satisfying trim constraints by changing the HTP angle of incidence at the given cruise Mach number.

The aerodynamic efficiency is optimized by performing a high-fidelity RANS simulation by solving the neg-Spalart Allmaras equation. The aerodynamic efficiency is calculated by taking the ratio of lift-coefficient to drag-coefficient where a constant lift-coefficient is used during CFD computations.

3.8.2 Design Variables

A total of 302 design variables are considered of which 301 design variables are from airfoil profiles of both fuselage and wing, twist angles of wing, airfoil profile of pylon, and engine integration sections. The 302nd design variable is for the HTP angle which is used for trimming.

Table 3.1: Design Variables

Design Variables Names	Number
Fuselage design variables	80
Wing design variables	140
Wing twist angles	6
Pylon design variables	20
Engine-Integration design variables	55
HTP angle of incidence	1
Total	302

Table 3.2: Reference Parameters

	Unit	Value
Reference Mach number	[-]	0.78
Reference Density	[Kg/ m^3]	0.33743
Reference Temperature	[K]	216.65
Reference Pressure	[Pa]	20985
Reference Area	[m^2]	348.1
Reference Length	[m]	5.35
Reference Point (x)	[m]	14.95

3.8.3 Problem Setup

The shape optimization method described in the above-mentioned process is applied to the Blended Wing Body half model, as the aerodynamic analysis is performed for the cruise condition. The computational domain is consisting of an unstructured mesh of the size of 4.2 million, which is generated on the ANSA for the baseline model. The optimization is realized for the design mission at an altitude of 11500m and at a cruise condition of Mach number 0.78. The reference parameters such as pressure, density, and temperature values that are required to compute the flow analysis are calculated using the altitude and Mach number from the website Aerospaceweb [30], and the remaining reference parameters are considered from the DLR-SIAM project which is mentioned in the section 1.2. These parameters are used for the flow computation throughout the optimization as emphasized in the table 3.2. For the flow convergence, the L^2 norm of TAU's density residual is considered by seven orders of magnitude. For each iteration, cost functions (objective function, constraints and their gradients) are computed and the FSQP algorithm is used to drive the optimization process. For the structural analysis, a full model with approximately 21000 mesh elements is used.

Chapter 4

Results

This chapter investigates the results of baseline configuration in section: 4.1 and optimization results in section: 4.2, in which two critical-designs points are compared in its subsections: 4.2.2 and 4.2.3 respectively along with their engine integration aspects in the subsection 4.2.1. In the last section: 4.3, coupled flow and structure analysis for critical-design points are investigated.

4.1 Baseline Model

A CFD computation is performed on the baseline model with the reference values taken from the SIAM project as shown in the section 3.8.3. Along with these parameters, the CFD computation is performed using the neg-Spalart Allmaras model, with a multigrid approach and CFL number 5. The Central scheme is used for flux discretization. The results of the flow computation for the baseline model are illustrated using the coefficient of pressure (C_p) contour along with the streamlines in the figure: 4.1. A huge shock is observed on the wing near the engine where the C_p value suddenly reduces. Due to this, the streamlines of the flow separation after the shock are also displayed. This is also verified on the coefficient of pressure (C_p) distribution in the figure: 4.2, where the graph is extracted at $Y = 10$ m from the symmetry plane. The results of the baseline model are shown in table 4.1. Since the computation is performed with a constant lift condition, the optimization is also expected to have same value for the coefficient of lift (C_L) and a reduction in the coefficient of drag (C_D).

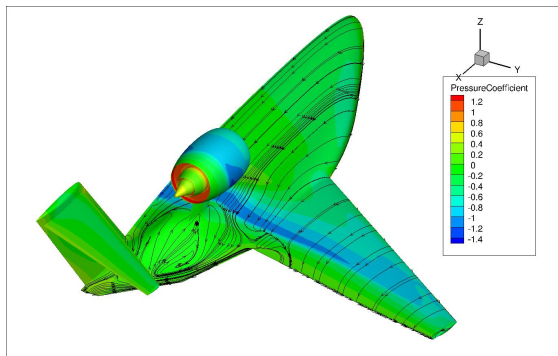


Figure 4.1: Baseline Model - Coefficient of Pressure (C_p) Contour

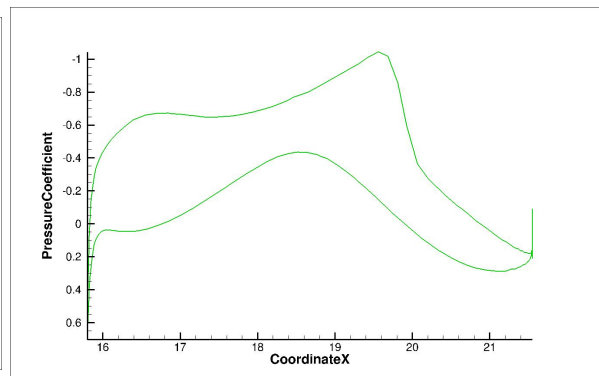


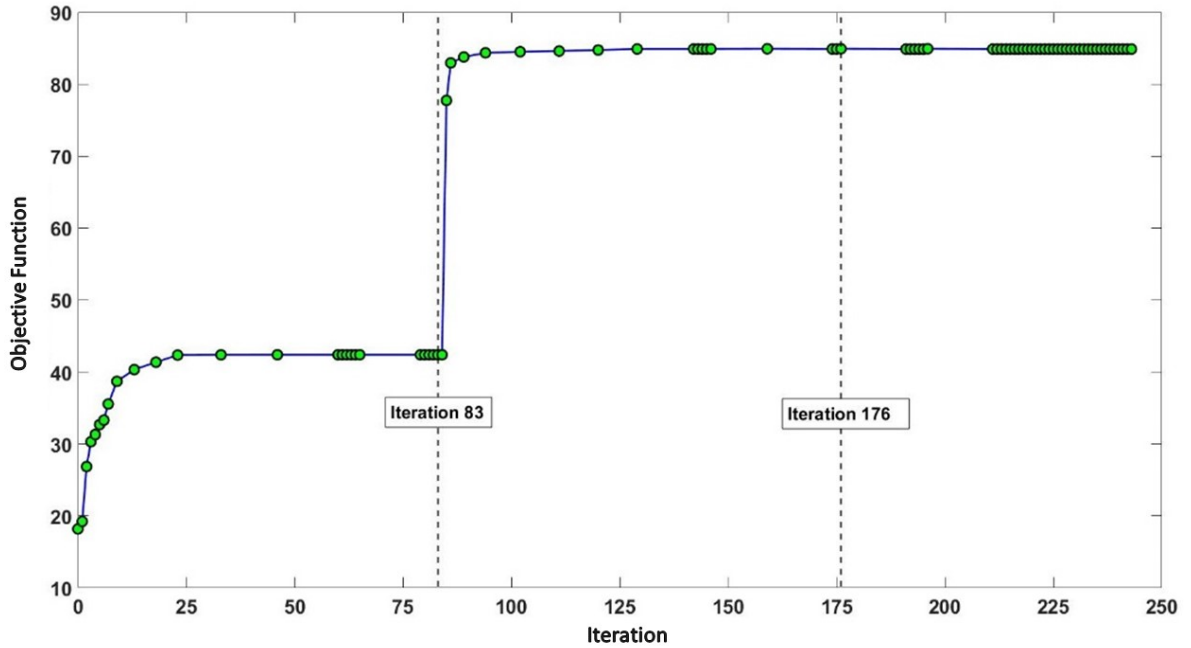
Figure 4.2: Baseline Model - C_p Distribution at $Y = 10$ m from Symmetry

Table 4.1: Baseline Model Results

	Unit	Value
Lift Coefficient	[-]	0.2312
Drag Coefficient	[-]	0.0252
Aerodynamic Efficiency	[-]	9.17
Breguet Range	[m]	1121481.99
Fuel Consumption	[Kg]	17988.69
Angle of Attack	[-]	0.921

4.2 Optimization

The baseline model is optimized based on the problem statement and design variables that are defined in section 3.8. The objective function of the optimization is to maximize the Aerodynamic Efficiency in which the coefficient of drag (C_D) is computed from both drag on the skin and the thrust from the engine. To validate these results, the critical-design points are recomputed using TAU with suitable drag computation which does not include thrust from the engine and only contains drag on the skin. The same values of upper bounds (X_{UB}) and lower bounds (X_{LB}) are used for optimization which were used while generating the CAD-ROMs (3.3). The optimization is an unconstrained optimization as trimming is implicit. Due to the absence of a suitable engine model to compute the thrust for the trim process, it was decided not to take trimming into account. The optimization history is plotted in the figure: 4.3.

**Figure 4.3:** Optimization History Plot

One can observe from the Figure: 4.3 that after iteration 83, there is a sudden jump in the objective function from 42 to 85. It is important to study the optimization iterations before and after the jump, to examine if there is any unphysical behavior due to the jump. Thus the following results will be a comparison between two iterations of 83 and 176 as shown in the figure. The objective of the optimization is to validate existing DLR - optimization codes with an unconventional aircraft configuration, in which the main focus was directed towards TAU computation, grid generation and parameterization of the CAD model, and the reduction of flow separation was not the primary focus of the optimization.

4.2.1 Engine Integration

The geometrical change in the engine integration section of the baseline model, the optimized model of iteration 83, and the optimized model of iteration 176 are compared below. The comparison is realized by plotting the Z- coordinate contour of the extracted engine integration sections.

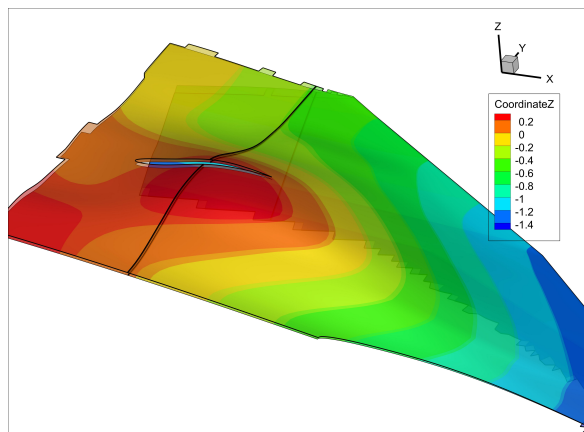


Figure 4.4: Baseline Model vs Optimized Model of Iteration 83 Engine Integration Effects

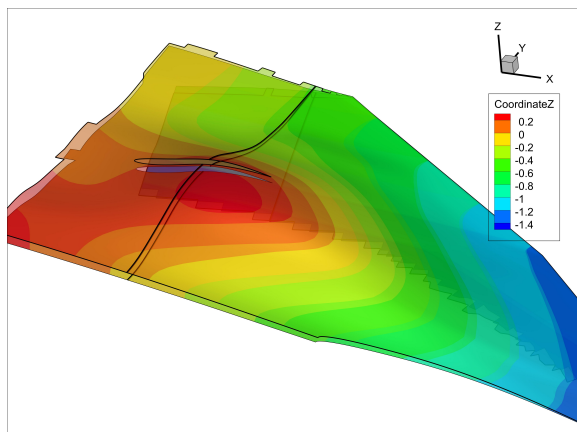


Figure 4.5: Baseline Model vs Optimized Model of Iteration 176 Engine Integration Effects

In the figure: 4.4, the baseline model is compared with the optimized model of iteration 83. The baseline model is located at the top with highlighted edges and a translucent effect, thus showing a distinctive reduction in the thickness of the geometry in iteration 83 which is generated by the CAD-ROM. The change in the model of iteration 83 can be clearly observed on the cross-sectional line along the engine integration section. A similar comparison is shown in the figure: 4.5, where optimized models of iteration 176 is compared again with the baseline model. Here is the baseline model again located at the top with highlighted edges and a translucent effect, thus showing a further reduction in the thickness of the geometry in iteration 176. This change in the model can be clearly detected on the cross-sectional line along the section.

4.2.2 Iteration 83

A CFD computation is performed again for the design parameters of Iteration 83 with the suitable boundary conditions to compute drag on the skin. This computation is compared to the baseline model in the figure: 4.6. In the comparison, it is evident that the shock generated for iteration 83 is significantly reduced when compared to the baseline model.

Table 4.2: Results Comparison for Iteration 83

	Unit	Baseline	Optimized Iteration 83
Lift Coefficient	[-]	0.2312	0.2311
Drag Coefficient	[-]	0.0252	0.0185
Aerodynamic Efficiency	[-]	9.17	12.44
Breguet Range	[m]	1121481.99	1544445.32
Fuel Consumption	[Kg]	17988.69	14140.47
Angle of Attack	[-]	0.921	1.909

The results of iteration 83 are shown in table 4.2, from which it is clear that the coefficient of lift (C_L) has not changed much, whereas a significant difference of 67 drag counts is observed, which is a 26.6% reduction in drag for the optimized iteration. Due to this reduction in drag coefficient

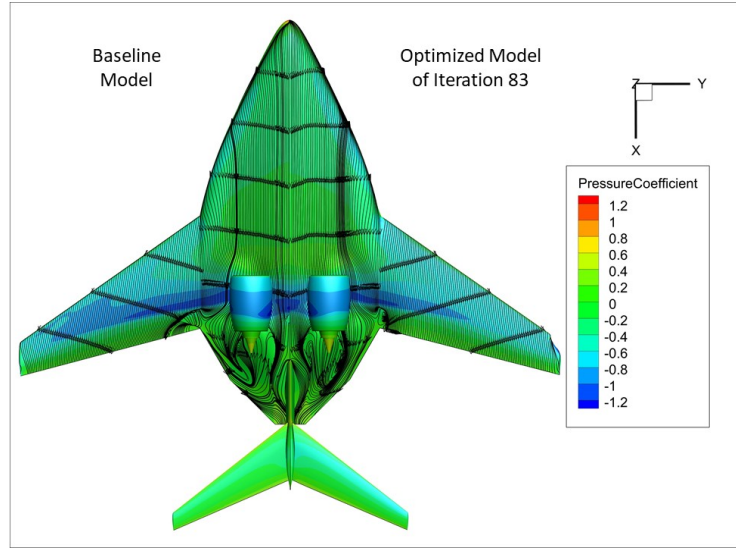


Figure 4.6: C_p Contour Comparison of Baseline Model vs Optimized Model for Iteration 83

(C_D), there is a 37.7% increase in range along with a 21% reduction in fuel consumption. The reduction in the shock is also evident from the figure: 4.7 which is taken at $Y = 10$ m from symmetry plane.

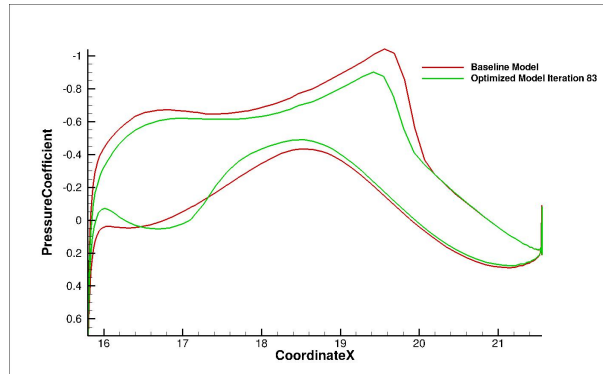


Figure 4.7: Comparison of (C_p) Distribution in Baseline Model and Optimized Model for Iteration 83 at $Y = 10$ m from Symmetry

For iteration 83 an interesting shape displacement field is generated on the wingtip, where a deformation can be observed when compared to the baseline model. Further investigation is carried out to find the origin of the wingtip deformation by remodeling the CAD parts with the new optimum design variables. Using this procedure, it is observed that the deformation in the wingtip is not originated from the CAD models, thus the resulting deformation must be generated by the CAD-ROM. To validate the result of the deformed wing tip, the modified CAD model which has the optimum design variables, is meshed again and another CFD computation is performed with the suitable boundary conditions which calculates the coefficient of drag (C_D) on the skin.

Table 4.3: Results Comparison of Iteration 83 - with- vs without- Wingtip Deformation

	Unit	Without Wing Deformation	With Wing Deformation
Lift Coefficient	[-]	0.2311	0.2311
Drag Coefficient	[-]	0.0225	0.0185
Aerodynamic Efficiency	[-]	10.27	12.44

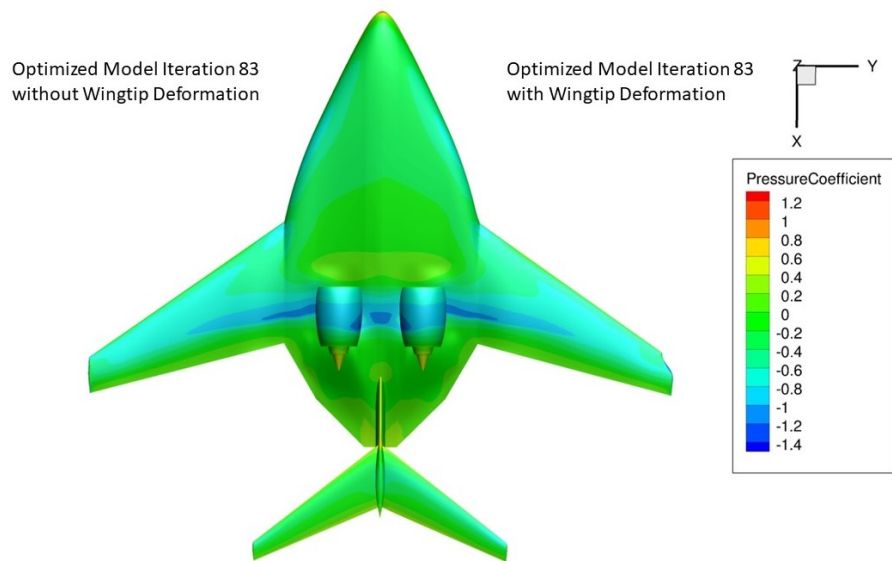


Figure 4.8: C_p Contour of Optimization Iteration 83 - with- vs without- Deformed Wingtip

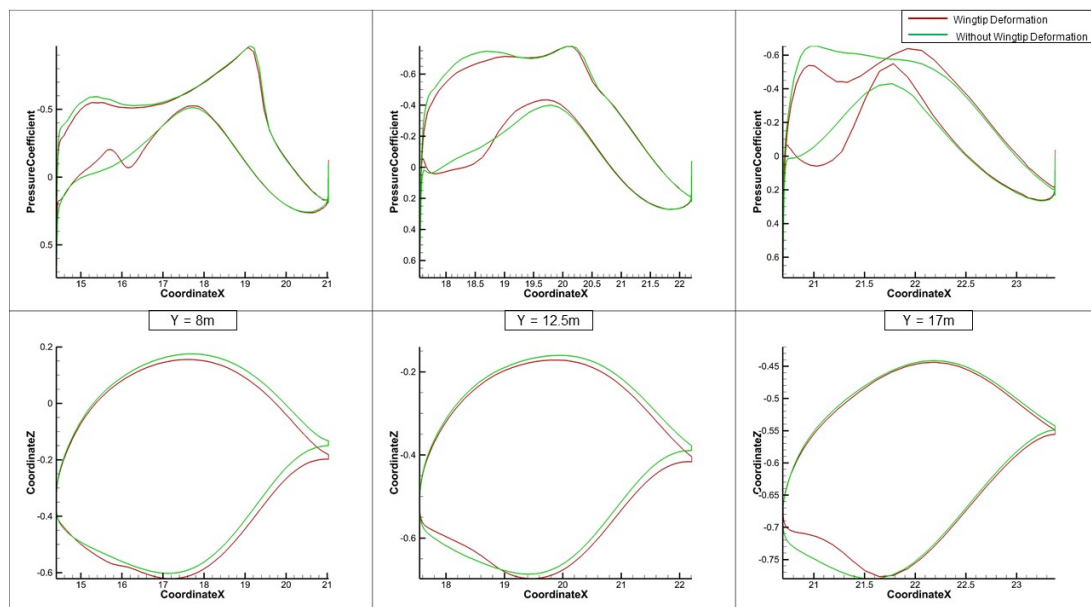


Figure 4.9: C_p Distribution Plots for Optimization Iteration 83 - with- vs without- Deformed Wingtip at $Y = 8, 12.5$ and 17m from Symmetry

In figure: 4.8, it is evident from the coefficient of pressure (C_p) contour that the shock generated in the modified CAD model which has no wingtip deformation, is very similar to the one with wingtip deformation. Although, the TAU computation for the updated CAD model which has no wingtip deformation has converged at a higher coefficient of drag (C_D) value, which can be observed in the table: 4.3. This is an increase of 40 drag counts for the same optimized model without the wingtip deformation, which is an increase of 21.6%.

To further analyze the difference between the two optimized shape models, the coefficient of pressure (C_p) distribution is plotted at three locations along the spanwise direction of the wing. The three locations are at $Y = 8$ (near wing root), 12.5 (middle of the wing), and 17 (near wingtip) meters from the symmetric plane, and the results are shown in the figure: 4.9. It is noticeable in the upper three graphs, that for the first two locations, the C_p distribution is very

close, but at the third location (which is near the wingtip), the C_p distribution is completely different. This could explain the difference in the coefficient of drag (C_D) for the two optimized models. On the other hand, when the geometry of the wing cross-section is compared in the bottom three graphs, the model with the wingtip deformation (generated by CAD-ROM) has a different geometry when compared to the model without the wingtip deformation (generated by remodeling CAD parts) at all locations. This might be due to the accuracy of CAD-ROM's shape displacement field.

4.2.3 Iteration 176

The Iteration 176 of the history plot is checked as it converged again after the sudden jump in objective function. A CFD computation is performed again for the design parameters of Iteration 176 with the suitable boundary conditions for drag computation on the skin and the result is compared to the previous result of Iteration 83.

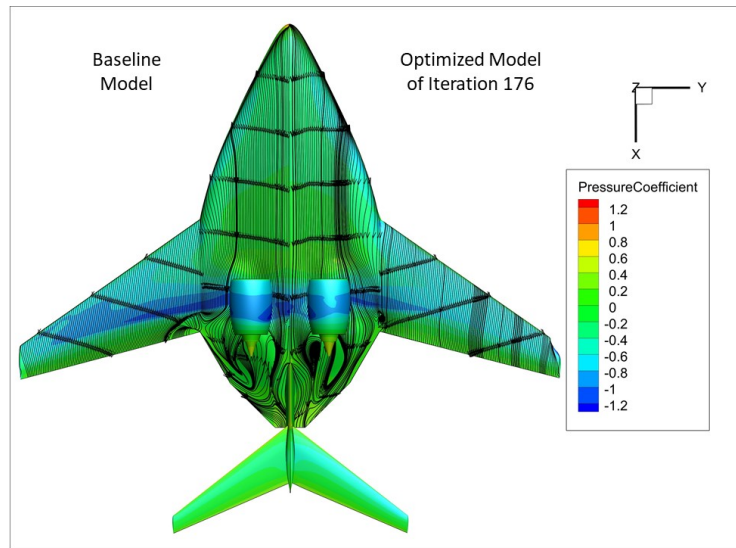


Figure 4.10: C_p Contour Comparison of Optimization Models for Iteration 83 vs Iteration 176

Table 4.4: Results Comparison for Iteration 176

	Unit	Optimized Iteration 83	Optimized Iteration 176
Lift Coefficient	[-]	0.2311	0.2311
Drag Coefficient	[-]	0.0185	0.0161
Aerodynamic Efficiency	[-]	12.44	14.305
Breguet Range	[m]	1544445.32	1774716.06
Fuel Consumption	[Kg]	14140.47	12653.46
Angle of Attack	[-]	1.909	2.053

It is noticeable from the figure: 4.10 that the shock near the engine has further reduced for this case, and the flow separation after the shock in the aft region is also reduced. This difference is also observed in the results table: 4.4. For Iteration 176 the coefficient of drag (C_D) has further reduced by 24 drag counts which is a 12.97% reduction in drag, thus increasing the range further by 12.98% and reducing the fuel consumption further by 10%. The reduction in shock can also be observed in the figure: 4.11. To investigate the difference in geometries between both models that resulted in the reduction in drag, both models are overlapped and shown in the figure: 4.12. For a more effective comparison, a section is extracted at $X = 18.5$ meters as shown in the previous figure and it is plotted along $Y-Z$ coordinate in the figure: 4.13.

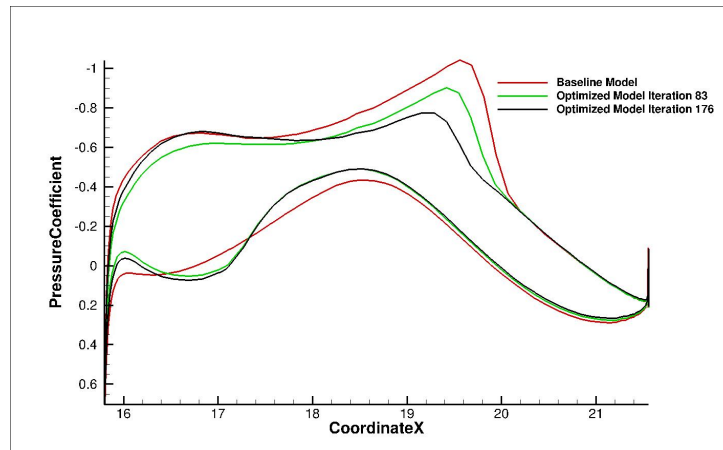


Figure 4.11: Comparison of C_p Distribution in Optimization Iteration 83 vs Optimization Iteration 176 at $Y = 10\text{m}$

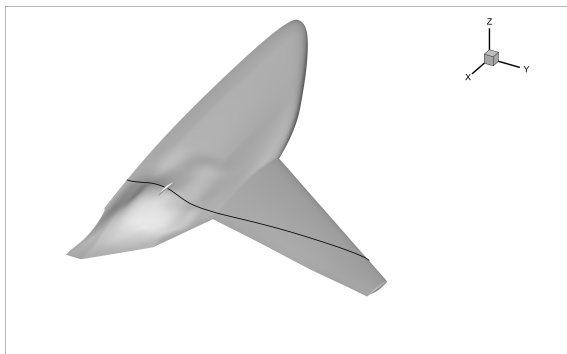


Figure 4.12: Optimized Model of Iteration 83 and Iteration 176 Shape Comparison

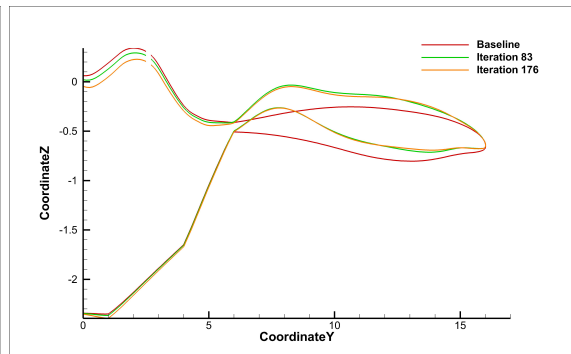


Figure 4.13: Optimized Model of Iteration 83 and Iteration 176 Shape Comparison at $X = 18.5\text{m}$

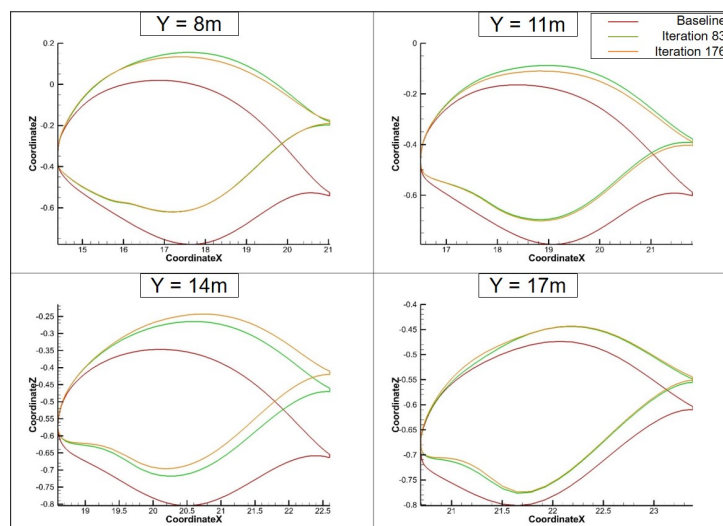


Figure 4.14: C_p Distribution Comparison of Optimization Models for Iteration 83 vs Iteration 176 at $Y = 8, 12.5$ and 17m from Symmetry

The noticeable reduction in thickness, near the engine integration section of the model for iteration 176 seems to be the reason for the further reduction in drag. In figure: 4.14 a comparison of airfoil sections between optimized models of iteration 83 and 176 is conducted at $Y = 8, 12.5,$

and 17 meters from the symmetry plane. It is evident that the airfoil shapes are similar, thus the further reduction in coefficient of drag (C_D) must be from the engine integration section.

Along with the reduction in the coefficient of drag (C_D), the optimized shape of Iteration 176 still has a wingtip deformation. Similar to the previous result in Iteration 83, the deformation in the wingtip is further analyzed by remodeling the CAD with updated design parameters and recomputing flow analysis.

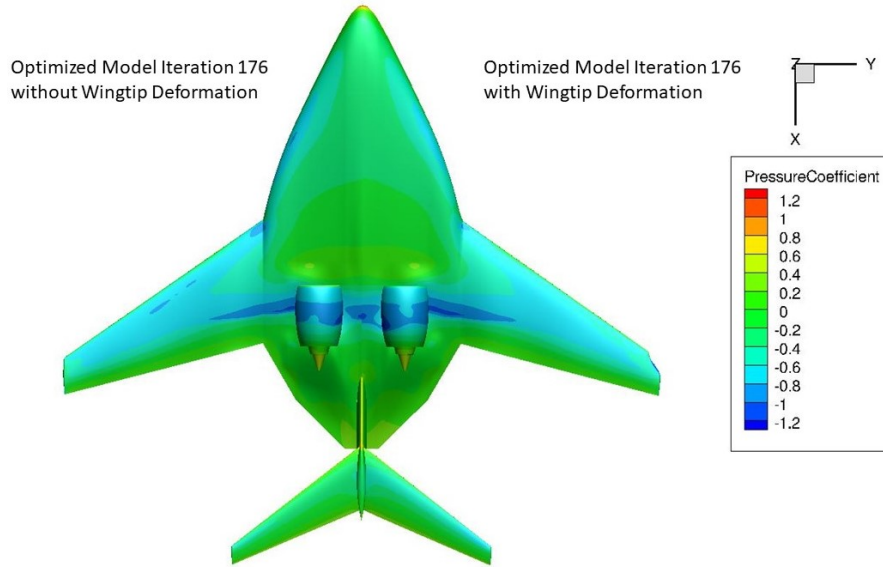


Figure 4.15: Comparison of C_p Contour for Optimization Iteration 176 with and without Wingtip Deformation

Table 4.5: Results Comparison of Iteration 176 - with- vs without- Wingtip Deformation

	Unit	Without Wing Deformation	With Wing Deformation
Lift Coefficient	[-]	0.2309	0.2311
Drag Coefficient	[-]	0.01995	0.0161
Aerodynamic Efficiency	[-]	11.56	14.305

Similar behavior is observed here when compared to the wingtip deformation of Iteration 83. From the figure: 4.15, it can be verified that the shock generated near the engine is very similar for both models, although the coefficient of drag (C_D) has significantly increased for the recomputed CAD model which has no wing tip deformation. The results are displayed in the table: 4.5, where the coefficient of drag (C_D) has increased by 38 drag counts which is an increase of drag by 23.9%.

A similar comparison is performed here when compared to Iteration 83, where three locations along the wing span are selected and the coefficient of pressure (C_p) distributions are plotted on the upper three graphs of the figure: 4.16. The locations are extracted at $Y = 8$ (near wing root), 12.5 (middle of the wing), and 17 (near wingtip) meters from the symmetry plane. At the first two locations, the C_p distributions are similar for both the cases of with- and without wingtip deformation. Whereas, at the third location, the C_p distribution is completely different. This change at the third location might explain the difference in drag computation. The bottom three plots show a change in the geometric cross-section of the wing. The difference in the cross-section might have been related to the accuracy of CAD-ROM's shape displacement field.

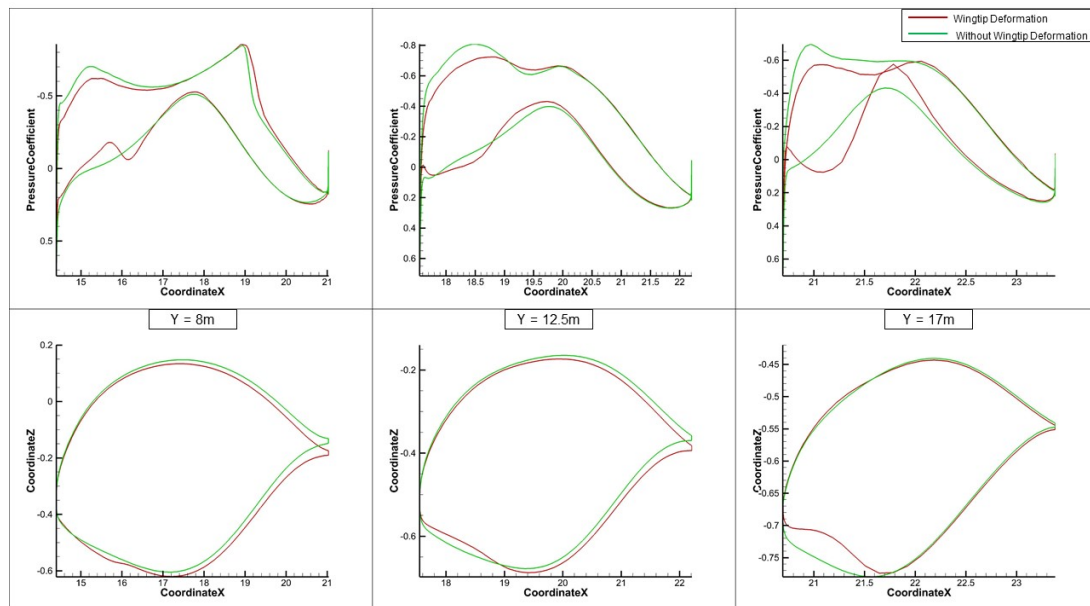


Figure 4.16: C_p Distribution Plots for Optimization Iteration 176 - with- vs without- Deformed Wingtip at $Y = 8, 12.5$ and 17m from Symmetry

4.3 CFD-CSM Coupling

To test the deformations due to the aerodynamic loads in the model, a CFD-CSM coupling on the Blended Wing Body model is conducted using the Airbus-Lagrange suite, where a Multidisciplinary Design Analysis (MDA) is performed on the critical design points of the previous shape optimization results, which are at baseline, Iteration 83, and Iteration 176. A structured mesh is generated using ANSA for the full-body model as shown in the section: 3.4. The leading edge and the trailing edge are excluded from the model since the deformation is expected to occur only on the wing box. For the computation of the structural deformation of the wing, the main wing model is assumed to deform and all other models of the BWB are fixed. The CFD-CSM coupling is performed for the suitable boundary conditions which can compute the drag on the skin by excluding the thrust. The MDA computation is trimmed with respect to α to achieve physically accurate results.

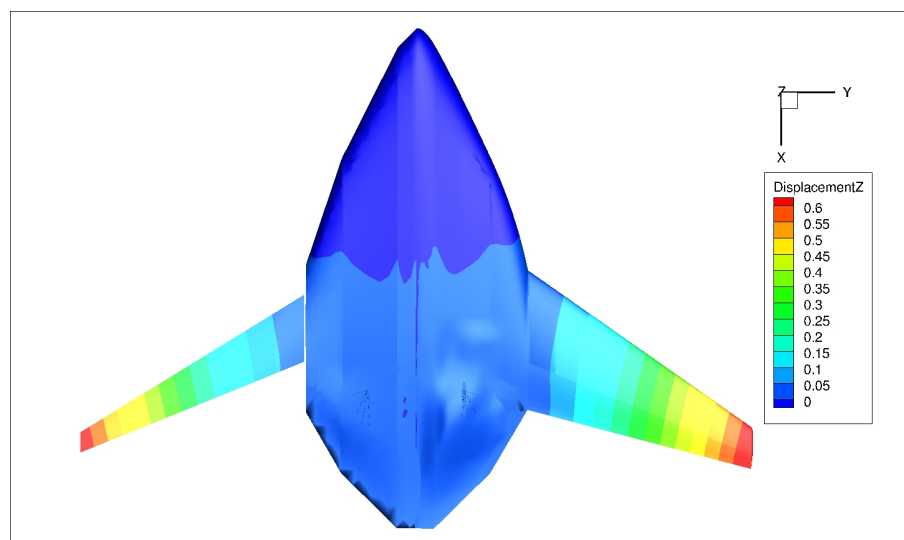
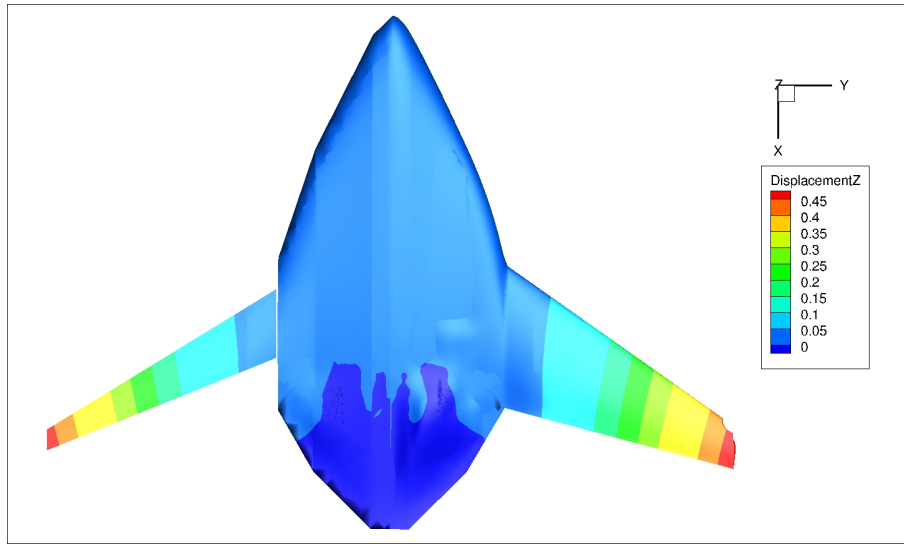


Figure 4.17: Deformation of the Baseline Model

Table 4.6: Results of CFD-CSM Coupling for Baseline Model

	Unit	Baseline Model CFD-CSM Coupling	Baseline Model Result
Displacement	[m]	0.6	-
Lift Coefficient	[-]	0.2308	0.2312
Drag Coefficient	[-]	0.0257	0.0252
Aerodynamic Efficiency	[-]	8.9667	9.17

Figure: 4.17 shows the displacement of the baseline BWB model along the Z- direction, where the CFD half model is overlapped on the right half of the CSM model. It is evident that in both models the displacement is similar with 0.6 m. As the model is trimmed with respect to α , the value of the coefficient of lift (C_L) is very similar to the CFD computation of the baseline which is shown in the table: 4.6. Whereas the drag coefficient shows a slight increase of 5 drag counts, which is an increase of 1.98% for the coupling case.

**Figure 4.18:** Deformation of the Iteration 83 Model**Table 4.7:** Results of CFD-CSM Coupling for Iteration 83 Model

	Unit	Iteration 83 Model CFD-CSM Coupling	Iteration 83 Model Optimized Result
Displacement	[m]	0.45	-
Lift Coefficient	[-]	0.23108	0.2311
Drag Coefficient	[-]	0.02262	0.0185
Aerodynamic Efficiency	[-]	10.2117	12.44

For the optimized model of Iteration 83, the displacement contour along the Z- direction is shown in the figure: 4.18, where the CFD half model is overlapped on the right half of the CSM model. The CFD-CSM coupling is implemented on the optimized Iteration 83 with wingtip deformation. The displacement for both the CFD and CSM models shows a similar displacement of 0.45 m and the results of CFD-CSM coupling are shown in the table: 4.7. The coefficient of lift (C_L) is very similar to the aerodynamic shape optimization result, whereas a higher coefficient of drag (C_D) is observed for the CFD-CSM coupling. This is an increase of drag by 22%.

The displacement along the Z- direction is computed for the optimized Iteration 176 as shown in the figure: 4.19, where the CFD half model is overlapped on the right side of the CSM full

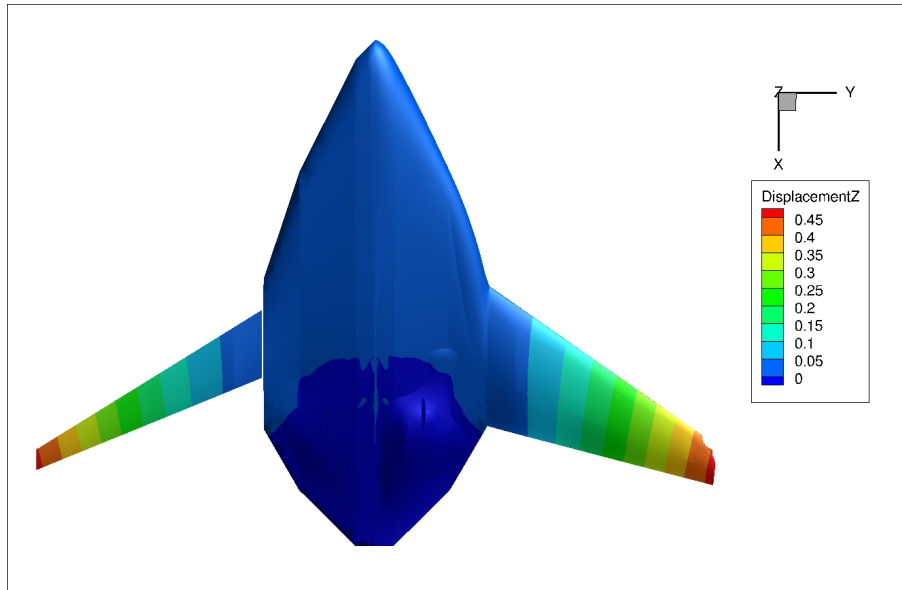


Figure 4.19: Deformation of the Iteration 176 Model

Table 4.8: Results of CFD-CSM Coupling for Iteration 176 Model

	Unit	Iteration 176 Model CFD-CSM Coupling	Iteration 176 Model Optimized Result
Displacement	[m]	0.45	-
Lift Coefficient	[-]	0.23103	0.2311
Drag Coefficient	[-]	0.02075	0.0161
Aerodynamic Efficiency	[-]	11.1307	14.305

model. It is evident that the displacement in both the models is very similar which is 0.45 m. The comparison of CFD-CSM coupling results and the respective aerodynamic shape optimization results are tabulated as: 4.8. It can be observed that the lift coefficient (C_L) is very similar in both cases and a significant difference of 46 drag counts is observed. This is an increase of 28.9% for the case of CFD-CSM coupling.

The structure model is optimized where it is sized according to two load cases of +2.5G and -1G. It has been observed that the structure model stays constant for all variations in the shape.

Chapter 5

Conclusion

Aerodynamic shape optimization is performed on the half model of the Blended Wing Body (BWB) with high-fidelity CFD computation including engine integration effects. It has been observed that the optimization has ran as expected showing that the DLR MDO chain which was tested many times for the tube-wing configurations also works for unconventional aircraft configurations. The history plot of the shape optimization is observed to have a sudden jump in the objective function, thus two critical design points are compared. As the decomposition of the drag during optimization was not performed, the critical design points are verified again with suitable drag computation thus calculating aerodynamic efficiency. The convergence history shows that the optimization was successful.

During the optimization the changes in the design shape were observed, across the wing section in both the airfoil shape and twist angles and the thickness of the engine integration section. Along with these changes deformation in the wingtip was also observed. This deformation is generated from the reduced order model of the parameterized geometry (CAD-ROM). To validate this change in geometry, the updated design parameters of the critical design points are extracted and remodeled in CAD, where, after performing the CFD computations, it is observed that the wingtip deformation did not originate from CAD models. The CFD computations also showed that the coefficient of drag (C_D) has significantly increased when compared to its counterparts which has wingtip deformation. The corresponding coefficient of pressure (C_p) distributions which were extracted at three locations along the span of the wing, showed similar distributions in the first two sections, whereas a completely different C_p distribution near the wingtip. The wing cross-sections are also plotted at these three locations, where a comparable difference exists between the two models of with- and without- wingtip deformation. The optimized models that were generated by the strange behavior of the CAD-ROM, seem to have produced better results

The study was also extended to perform MDA on the BWB full model where a high-fidelity CFD-CSM coupling is performed along with trimmed AoA. The results of coupling show displacement along the vertical direction, as a result of which an increase in the coefficient of drag (C_D) is observed. Whereas the coefficient of lift (C_L) remains constant for all the cases. Similar to the increasing trend of the aerodynamic efficiency for the critical design points of shape optimization, the aerodynamic efficiency of the MDA is also increasing. This shows that the MDA provides better physical representation of the problem as it includes the interaction between the effects of one discipline with the other.

The results of the shape optimization at Iteration 176 showed the best result among them all, where the optimized result is 36.6% less in coefficient of drag (C_D) when compared to the baseline model. As the scope of the study is for aerodynamic shape optimization, the results can be further investigated by performing an MDO for better comprehensive results. As the baseline model was from the DLR-SIAM project, whose major goal was reduction of the noise

impact, the flow separation was initially not reduced. As the optimization is sensitive to the baseline model and the focus was on the methodology, the flow separation could not be reduced during the optimization as well. The future work can be realised to be more focused on reducing flow separation by better parameterization of the pylon and engine integration with its specific constraints, along with constraints on the angle of attack. It is also important to validate the shape displacement field reconstruction of the CAD-ROM for higher accuracy.

Bibliography

- [1] Pranav Mahamuni, A. Kulkarni, and Yash Parikh. Aerodynamic study of blended wing body. 9, 01 2014.
- [2] Doukaini Mavroudi, Anestis Kalfas, Acher-Igal Abenheim, and Hany Moustapha. Design optimization of aero-engine turbine blade and disc fixing. *Aeronautics and Aerospace Open Access Journal*, 3(2):106 – 113, Jun 2019.
- [3] Airline industry - number of flights, August 2023.
- [4] ARCS – Austrian Research Centers GmbH. Flightpath 2050: Europe’s vision for aviation. https://www.arcs.aero/sites/default/files/downloads/Bericht_Flightpath_2050.pdf, August 2023.
- [5] Zhenli Chen, Zhang Minghui, Yingchun Chen, Weimin Sang, Zhaoguang Tan, Dong Li, and Binqian Zhang. Assessment on critical technologies for conceptual design of blended-wing-body civil aircraft. *Chinese Journal of Aeronautics*, 32, 07 2019.
- [6] Michael Iwanizki, Dennis Keller, Florian Schmidt, Yasim Julian Hasan, Joscha Kurz, Felix Wienke, Lothar Bertsch, Michael Möfner, Philip Balack, Jannik Häßy, and Benjamin Fröhler. Conceptual aircraft design activities related to blended wing body configurations in the scope of the dlr project siam. *9th European Conference for Aeronautics and Space Sciences*, 2022.
- [7] Michael Pott-Pollenske, Daniela Almoneit, Heino Buchholz, and Henri Siller. Low noise atra – an aircraft noise reduction study based on retro-fit technologies. In *2021 AIAA AVIATION Forum and Exposition*, August 2021.
- [8] R. H. Liebeck. Design of the blended wing body subsonic transport. *Journal of Aircraft*, 41(1):10 – 25, 2004.
- [9] Edwin Ordoukhanian and Azad M. Madni. Blended wing body architecting and design: Current status and future prospects. *Procedia Computer Science*, 28, 2014.
- [10] Airbus. Airbus reveals its blended wing aircraft demonstrator, Feb 2020.
- [11] Bombardier. Bombardier achieves important milestones on ecojet research project, continues industry-defining work toward sustainable aviation, May 2023.
- [12] Guy Norris and Graham Warwick. Jetzero unveils midmarket airliner and air force tanker bwb plan, Apr 2023.
- [13] T. Gerhold, M. Galle, O. Friedrich, and J. Evans. Calculation of complex three-dimensional configurations employing the dlr-tau-code. *35th Aerospace Sciences Meeting and Exhibit*, 1997.
- [14] Dieter Schwamborn, Anthony Gardner, Heiko von Geyr, Andreas Krumbein, Heinrich Lüdeke, and Arne Stürmer. Development of the tau-code for aerospace applications, Jan 1970.

- [15] Cadence CFD. What is the spalart-allmaras turbulence model?, Oct 2022.
- [16] Steven R. Allmaras, Forrester T. Johnson, and Philippe R. Spalart. Modifications and clarifications for the implementation of the spalart-allmaras turbulence model, Jul 2012.
- [17] BETA CAE Systems. The advanced cae pre-processing software for complete model build up.
- [18] A. A. Gastaldi, F. Volle, F. Daoud, and C. Breitsamter. Simultaneous airframe shape and sizing optimization using flowsimulator and the lagrange mdo suite.
- [19] Thomas A. Zang and Lawrence L. Green. Multidisciplinary design optimization techniques: Implications and opportunities for fluid dynamics research, Jul 1999.
- [20] Ideen Sadrehaghighi. *Aircraft Multidisciplinary Design & Optimization (MDO)*. 02 2023.
- [21] Catia documentation. http://catiadoc.free.fr/online/cfyugfss_C2/cfyugfssut0202.htm. Accessed on [30-07-2023].
- [22] Dominic Masters, NJ Taylor, Thomas Rendall, Christian Allen, and Daniel Poole. A geometric comparison of aerofoil shape parameterisation methods. *AIAA Journal*, January 2017.
- [23] D. Barral, J.-P. Perrin, E. Dombre, and A. Liegeois. An evolutionary simulated annealing algorithm for optimizing robotic task point ordering. In *Proceedings of the 1999 IEEE International Symposium on Assembly and Task Planning (ISATP'99) (Cat. No.99TH8470)*, pages 157–162, 1999.
- [24] A. Merle, P. Bekemeyer, S. Görtz, S. Keye, and L. Reimer. Adjoint high-dimensional aircraft shape optimization using a cad-rom parameterization. *CEAS Aeronautical Journal*, 2023.
- [25] Kamil Bobrowski, Esteban Ferrer, Eusebio Valero, and Holger Barnewitz. Aerodynamic shape optimization using geometry surrogates and adjoint method. *AIAA Journal*, 55(10):3304 – 3317, 2017.
- [26] M. D. McKay, R. J. Beckman, and W. J. Conover. A comparison of three methods for selecting values of input variables in the analysis of output from a computer code. *Technometrics*, 21(2):239–245, 1979.
- [27] Sebastian Burhenne, Dirk Jacob, Gregor P Henze, et al. Sampling based on sobol sequences for monte carlo techniques applied to building simulations. In *Proc. Int. Conf. Build. Simulat.*, pages 1816–1823, 2011.
- [28] Andrei Merle, Andreas Ronzheimer, Peter Bekemeyer, Stefan Görtz, Sebastian Keye, and Laura Reimer. Gradient-based optimization of a flexible long-range transport aircraft using a high-dimensional cad-rom parameterization.
- [29] Andrei Merle, Caslav Ilic, Mohammad Abu-Zurayk, Jannik Häßky, Richard-Gregor Becker, Matthias Schulze, and Thomas Klimmek. High-fidelity adjoint-based aircraft shape optimization with aeroelastic trimming and engine coupling. *Journal of Aerospace Engineering*, 2023.
- [30] Atmospheric calculator. <https://aerospaceweb.org/design/scripts/atmosphere/>. Accessed on [05-08-23].